Magmatic Activity and Dynamics of Melt Supply of Volcanic Centers of Ultraslow Spreading Ridges: Hints From Local Earthquake Tomography at the Knipovich Ridge

M. Meier[1,2,3] , **V. Schlindwein[1,2]**, and **F. Schmid[4,5]**

[1]Alfred Wegener Institute, Helmholtz Centre for Polar and Marine Research, Bremerhaven, Germany, [2]Faculty of Geosciences, University of Bremen, Bremen, Germany, [3]Now at K.U.M. Umwelt- und Meerestechnik Kiel GmbH, Kiel, Germany, [4]Geomar, Helmholtz Centre for Ocean Research Kiel, Kiel, Germany, [5]Now at Technical University of Munich, Munich, Germany

Abstract Along ultraslow spreading ridges melt is distributed unequally, but melt focusing guides melt away from amagmatic segments toward volcanic centers. An interplay of tectonism and magmatism is thought to control melt ascent, but the detailed process of melt extraction is not yet understood. We present a detailed image of the seismic velocity structure of the Logachev volcanic center and adjacent region along the Knipovich Ridge. With travel times of P- and S-waves of 3,959 earthquakes we performed a local earthquake tomography. We simultaneously inverted for source locations, velocity structure and the Vp/Vs-ratio. An extensive low velocity anomaly coincident with high Vp/Vs-ratios >1.9 lies underneath the volcanic center at depths of 10 km below sea level in an aseismic area. More shallow, tightly clustered earthquake swarms connect the anomaly to a shallow anomaly with high Vp/Vs-ratio beneath the basaltic seafloor. We consider the deep low-velocity anomaly to represent an area of partial melt from which melts ascent vertically to the surface and northwards into the adjacent segment. By comparing tomographic studies of the Logachev and Southwest Indian Ridge Segment-8 volcano we conclude that volcanic centers of ultraslow spreading ridges host spatially confined, circular partial melt areas below 10 km depth, in contrast to the shallow extended melt lenses along fast spreading ridges. Lateral feeding over distances of 35 km is possible at orthogonal spreading segments, but limited at the obliquely spreading Knipovich Ridge.

Plain Language Summary Mid-ocean ridges mark the tectonic plate boundaries, where the plates drift apart. Fresh magma rises into the gap and builds new seafloor. The slower the plates drift apart, the less magma is present underneath the ridge. At very slow spreading ridges there is not enough magma to build new seafloor along the entire length of the ridge. Rather, melt is guided toward individual volcanic centers spaced at about 100 km, where melt accumulates and ascents. In our study we try to find melt storage areas and ascent paths of such a volcanic center. With velocities of different seismic wave types from earthquakes we map the velocity structure of the area underneath the major Logachev volcanic center. Lower velocities indicate an area partly including melt at depths of more than 10 km, far deeper than at mid-ocean ridges with sufficient melt supply. From the deep magma reservoir, many earthquake swarms map the long ascent path of melt to the surface. The interplay of magmatic and tectonic activity is important here. In a comparison with results from another volcanic center, we find that lateral magma feeding is possible in orthogonal spreading, but limited in oblique spreading, as at the Knipovich Ridge.

1. Introduction

Ultraslow spreading ridges with spreading rates below 20 mm/yr exhibit different characteristics and behavior than any faster spreading ridges (Dick et al., 2003). At ultraslow pace, melt supply is not high enough to sustain a spatially continuous shallow melt reservoir underneath the rift valley and therefore volcanic activity and magmatism do not occur along the entire rift axis. Instead, they are bound to distinct regions along the ridge that receive more melt than the ridge on average does (Cannat et al., 2003; Standish et al., 2008). Those magmatic segments build volcanic centers that are widely spaced, often by several tens of kilometers (Cannat et al., 2003; Curewitz et al., 2010; Standish et al., 2008). Volcanic centers receive enough melt to build volcanic edifices in the rift valley. If the melt supply persists over time, seamount chains or a line of elevations form in spreading direction (Jokat et al., 2003; Mendel et al., 2003) (e.g., Figure 1b). The regions in between volcanic centers are dominated
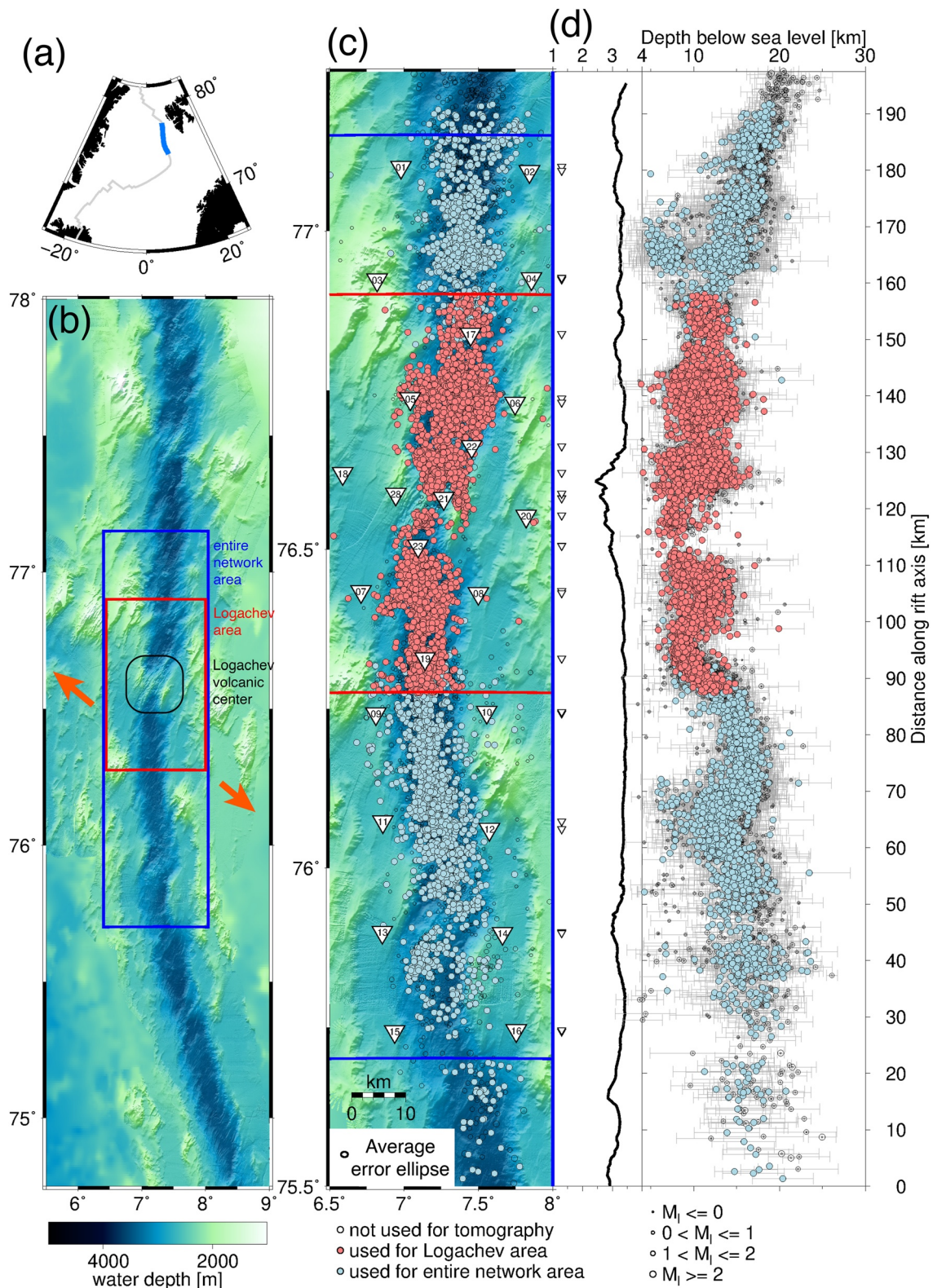
Figure 1.

by tectonism. At amagmatic segments, mantle rocks are exposed at the seafloor, while at magmatic segments basaltic seafloor is found (Michael et al., 2003). Melt focusing is the inferred underlying process leading to the uneven melt distribution along ultraslow spreading ridges (Cannat et al., 2003; Sauter & Cannat, 2010). It guides melt from amagmatic segments along the lithosphere - asthenosphere boundary toward magmatic segments and their volcanic centers (Standish et al., 2008). Evidence for a strongly undulating brittle–ductile boundary (approx. 650 ± 100°C isotherm (Anderson, 1995; McKenzie et al., 2005)) with thin lithosphere underneath volcanic centers was found in seismicity studies of Meier et al. (2021), Schlindwein and Schmid (2016) and Schmid and Schlindwein (2016). Melt traveling along-axis along an isotherm-parallel permeability boundary toward the volcanic centers therefore appears to be a common mechanism at ultraslow spreading ridges. The permeability boundary forms when molten material starts crystallizing at the base of the lithosphere at temperatures of 1000–1300°C (Cannat, 1996) and thereby prevents further melt ascent.

Little is known about how melt at ultraslow spreading ridges is extracted and ascents at volcanic centers. Standish et al. (2008) and Montési et al. (2011) speculate that faults play a major role in allowing magma ascent. Indeed, Müller and Jokat (2011), Tolstoy et al. (2001) and Schmid et al. (2017) found that earthquake swarms with magnitudes even larger than magnitude 5 preceded phases of magmatic activity at the ultraslow Gakkel and Southwest Indian Ridges. Magmatic segments show a thin carapace of basalt on the seafloor also away from volcanic centers. Montési et al. (2011) postulate that magma is redistributed at crustal levels through fault systems to erupt on the seafloor also at larger distances from the volcanic centers. The complex interaction between magmatic and tectonic activity remains poorly understood, but likely plays a central role in lithospheric accretion at ultraslow spreading ridges. In this study we therefore combine a seismicity analysis with a local earthquake tomography to image in detail the structure of an ultraslow spreading volcanic center, its plumbing system and ongoing magmatic and tectonic spreading processes.

Local earthquake tomography (LET) studies of volcanoes detected magma chambers and partial melt areas (Indrastuti et al., 2019; Koulakov et al., 2020), dikes and magma conduits (Koulakov et al., 2017), where eruption material is transported. Also, gas saturated areas as part of hydrothermal systems (Koulakov et al., 2020) and cooled intrusive bodies (Syracuse et al., 2015) that are fractured (Indrastuti et al., 2019) have been identified from LET results. In general, the interpretation of the resulting velocity structure is complex and often ambiguous without additional information on the subsurface (Indrastuti et al., 2019). At faster spreading ridges, tomography studies yielded evidence for hydrothermal circulation for example, at the Juan de Fuca Ridge (Kim et al., 2019). A seismic refraction tomography by Dunn et al. (2017) detected normal faulting at the Mid-Atlantic Ridge in addition to a near-surface zone of fluid-rock alteration. To date, tomography studies at ultraslow spreading ridges are rare. Korger and Schlindwein (2014) detected a low velocity body at the location of a volcanic center on Gakkel Ridge and suggested that it is caused by warm intrusions. However, this study was based on a few weeks long survey with seismic receivers placed on drifting sea ice floes and has a limited resolution. Schmid et al. (2017) conducted a local earthquake tomography study at a volcanic center, the Segment-8 volcano, along the ultraslow spreading Southwest Indian Ridge, using 10 months of seismicity data from an ocean bottom seismometer network with a wide station spacing of about 15 km. Schmid et al. (2017) found the first convincing evidence for a region of partial melts underneath an ultraslow spreading ridge volcanic center. With our LET study of the Knipovich Ridge, based on a densely spaced network of ocean bottom seismometers (Figure 1), we provide new insights at unprecedented detail into the structure and dynamics of the major volcanic centers of ultraslow spreading ridges.

2. Geological Setting

The Knipovich Ridge is an ultraslow spreading ridge with a full spreading rate of 14–17 mm/yr and is part of the Arctic Ridge System (Figure 1a). The ridge is characterized by high obliquity with an angle of 35–50° between the spreading direction and the ridge axis trend (Curewitz et al., 2010; DeMets et al., 2010; Okino et al., 2002)

Figure 1. Overview of the study area and seismicity at the Knipovich Ridge. (a) Marks plate boundaries as gray line and section of the Knipovich Ridge in (b) in blue. (b) Shows the bathymetry of the region, the spreading direction of the Knipovich Ridge as orange arrows and the sub-study areas. In (c) the northern and southern boundaries of the sub-study regions are given as colored lines in E-W. Circles indicate reliably located earthquakes from Meier et al. (2021), light-red circles are used for tomography of the Logachev area, light-blue and additional light-red circles for the entire network area. The size of the circles corresponds to local magnitude, M_l. In the lower left corner the average error ellipse is given. Ocean bottom seismometer stations are depicted as white triangles with the station numbers. Analogously, (d) shows the elevation and seismicity pattern with gray depth error bars along the 7.25°N cross section.

(Figure 1). The Knipovich Ridge extends in N–S direction for around 500 km between the Molloy transform fault in the North and the Mohns-Knipovich Bend in the South. Along the Knipovich Ridge, several volcanic centers were identified through morphological, gravimetric and magnetic measurements (Curewitz et al., 2010; Okino et al., 2002). The major volcanic centers are spaced by 60–110 km along the ridge (Hellevang & Pedersen, 2005) and often continue as seamount chains in spreading direction to both sides of the ridge (Curewitz et al., 2010), indicating stable magmatic activity for the last 7–8 Ma (Hellevang & Pedersen, 2005). The most prominent volcanic center is the Logachev volcanic center (Figure 1b), elevated up to 1,000 m above the rift valley floor (Curewitz et al., 2010). At its northern flank, Elkins et al. (2014) found fresh basaltic samples dredged from the seafloor indicating recent activity of the Logachev volcanic center. While magmatically active ridge parts have no or very little sedimentary cover and are therefore accessible to geological sampling, tectonically dominated ridge parts are covered by up to 500–1,000 m thick sediments (Amundsen et al., 2011; Kvarven et al., 2014). Sediments also cover the rift flanks. There is 800–1,000 m sediment thickness on the western flank and up to 1,500 m on the eastern rift flank (Kvarven et al., 2014), with sediments originating from the continental shelf east of the Knipovich Ridge.

Along ultraslow spreading ridges, German et al. (1998) found unexpectedly high hydrothermal activity. The most prominent site of hydrothermal activity at the Knipovich Ridge is the Loki's Castle vent field at the bend to Mohns Ridge in the south at 73.5°N (Pedersen et al., 2010). Further north, three additional vents sites are inferred by plumes and trace elements in the seawater at 74.8°N, 76.78°N and 77.63°N (Connelly et al., 2007; Hahm et al., 2004; Sundvor, 1997; Tamaki et al., 2001), but their seafloor locations are unconfirmed.

Based on the seismicity pattern Meier et al. (2021) defined sections of the Knipovich Ridge with magmatic and amagmatic characteristics. We use LET to study the subsurface velocity structure and get insights into the geological structure at the magmatic section underneath and around the Logachev volcanic center depicted in Figure 1. The study is based on data from twelve ocean bottom seismometers spaced by about 10 km. Additionally, we perform a tomographic study of the entire network of 24 ocean bottom seismometers with larger spacing to get a broader overview of the velocity structure of an ultraslow spreading ridge.

3. Methods

3.1. Local Earthquake Tomography

The seismicity data were recorded for 11 months by 24 ocean bottom seismometers deployed along 160 km of the Knipovich Ridge. The earthquakes are manually picked by an experienced analyst and located with HYPOSAT (Schweitzer, 2001, 2018) using a 1D velocity model, which is determined with PyVelest on the basis of a subset of events (Kissling, 1995; https://github.com/saeedsltm/PyVelest). The 1D velocity model is used as input for the tomographic inversions. The earthquake pattern is robust, also when locating with a different location algorithm (Meier et al., 2021). More detailed information on the processing steps of earthquake detection, phase picking and location using a 1D velocity model are described in Meier et al. (2021). Assumed pick uncertainties are 0.02 and 0.1 s for impulsive and 0.05 and 0.2 s for emergent P and S phase picks, respectively.

We performed the tomography for two different subregions, one for the area around the Logachev volcanic center (that we term here Logachev area) and one for the entire study area along the rift axis (which we term entire network area). We used these two subregions, because we have a higher network density around the Logachev volcanic center, which allows for a higher model resolution. Furthermore we are able to evaluate effects at the boundaries of the smaller subregions. We selected events for the tomographic inversions from the earthquake catalog of Meier et al. (2021) that includes in total 14,401 located earthquakes with local magnitudes up to 3.2. For the tomographic inversion of the Logachev area, only events that occurred between 76.275°N and 76.9°N were used, for the entire network area we enlarged this to be between 75.5°N and 77.2°N. We selected only events that were considered as reliably located in Meier et al. (2021), which required that the hypocenter depth could be determined with a maximum error of 5 km, the 95% error ellipse (Smajor) had a mean length of maximum 5 km and travel time residuals had a maximum root-mean-square (RMS) error of 0.4 s. From this subset of events, we further selected only those events that have at least 7 phase picks in case of the Logachev area, and at least 10 phase picks for the entire network area. Station KNR28 had noisy data that included numerous gaps, but as it was positioned directly west of the Logachev volcanic center, it was therefore an important station for the tomography model. P-phases on this station were mainly picked if hydrophone and vertical seismometer channels

consistently showed an onset. Hence, P-phase arrival times were considered sufficiently trustworthy, but S-phase picks were excluded. In addition, we used only P-phase picks if their travel time residual was less than 0.4 s in the initial location. This procedure ensured that incorrect picks, resulting from multiple P onset options from station KNR28, could be excluded. The P-phase travel times of station KNR28 were not counted to reach the minimum number of phases required for the event to be used (minimum 7 or 10 phase picks) and were therefore additional. Similarly, station KNR21 situated directly on top of the Logachev volcanic center was included despite its slightly non-linear clock drift, affecting mostly the time from October 2016 until May 2017. We approximated this non-linearity by an additional static station correction of 0.2 s for this time period. In total, we used 5,775 events with 86577 phase picks (41132 P- and 45445 S- phases) for the entire network area and 3,959 events with 44345 phase picks (22699 P- and 21646 S- phases) for the Logachev area.

For the tomographic inversion, the LOTOS code (Koulakov, 2009) was used that is able to invert for P- and S-wave velocity structures, Vp/Vs-ratio and source locations simultaneously. In a first step, LOTOS locates the events in an initial 1D velocity model using straight ray paths. The initial 1D velocity model is the same as in Meier et al. (2021). In the next step the events are located in a 3D velocity model using a bending tracing algorithm. For the boundary between seafloor and water, that is implemented in this step, we used the bathymetry data with 100 m grid resolution from Meier et al. (2021). The tomography model grids are constructed by nodes spaced at 1 km in horizontal direction and at variable node spacing of 1 km maximum in vertical direction depending on the ray coverage. We used four grids with different azimuthal orientations to minimize grid related effects on the results. The grids are oriented at 0°, 22°, 45° and 67° from north and the resulting velocities at the individual grid nodes are averaged at the end of each iteration. Each consecutive iteration starts again by locating the events based on the updated 3D velocity model. After five iterations no significant reduction of the RMS residuals was achieved. We determined the controlling parameters such as the weights for source shifts, amplitude damping and smoothing based on the results of the synthetic tests.

3.2. Synthetic Tests

3.2.1. Checkerboard Tests

We performed several checkerboard tests to optimize parameters such as weighting, smoothing and damping and to estimate the resolution capability of both tomography model regions. The earthquake locations were used from the last iteration of the real data case to calculate the synthetic travel times using the 3D ray tracing. Additional noise was added to the data, by raising the final iterations' travel time residuals by 10% for P-phases and 15% for S-phases and adding this to the data. With this synthetic data as input the tomographic inversion is performed in the same way as with the real data. We separately tested the horizontal and vertical resolution capability of our model (Figures 2, 3 and Figures S1 and S2 in Supporting Information S1).

For the horizontal test, we used vertical cuboids with ±7% alternating velocity anomaly with opposite signs for P- and S-wave models. The cuboids span the entire study area depth and vary in their base area. Figure 2 shows the results of the horizontal checkerboard test for the Logachev area. The checkerboard test results of the entire network area are included in Figure S1 in Supporting Information S1. With a side length of 8 km of the cuboids and 2 km spacing between them, the synthetic test could recover the checkerboard pattern of the input anomalies. When reducing the side length of the cuboids to 5 km, the resolution is still good in the central part of the study area, but reduces toward the edges and at larger depth. In both cases the best recovery is warranted in the depth interval of 8–10 km below sea level.

With a second checkerboard test we estimated the vertical resolution capability of our tomography model (Figure 3). Here, horizontal cuboids were used that span the entire E-W area of the model, such that they lie perpendicular to the vertical cross sections along the rift axis. The cuboids have ±7% alternating velocity anomalies with opposite signs for P- and S-wave models. The vertical checkerboard test for the Logachev area is displayed in Figure 3. Figure S2 in Supporting Information S1 shows the checkerboard test for the entire network area. The vertical resolution of the tomographic models is in general not as good as the horizontal, since here the trade-off between velocity and source parameters becomes more important and the geometry of sources and receivers is less favorable than in the horizontal dimension. The vertical checkerboard shows that toward the edges of the inversion area the resolution decreases (Figure 3). In the central part, where the earthquakes are densely spaced, the resolution capability is good, as well as in the shallower parts. In the seismicity gap between
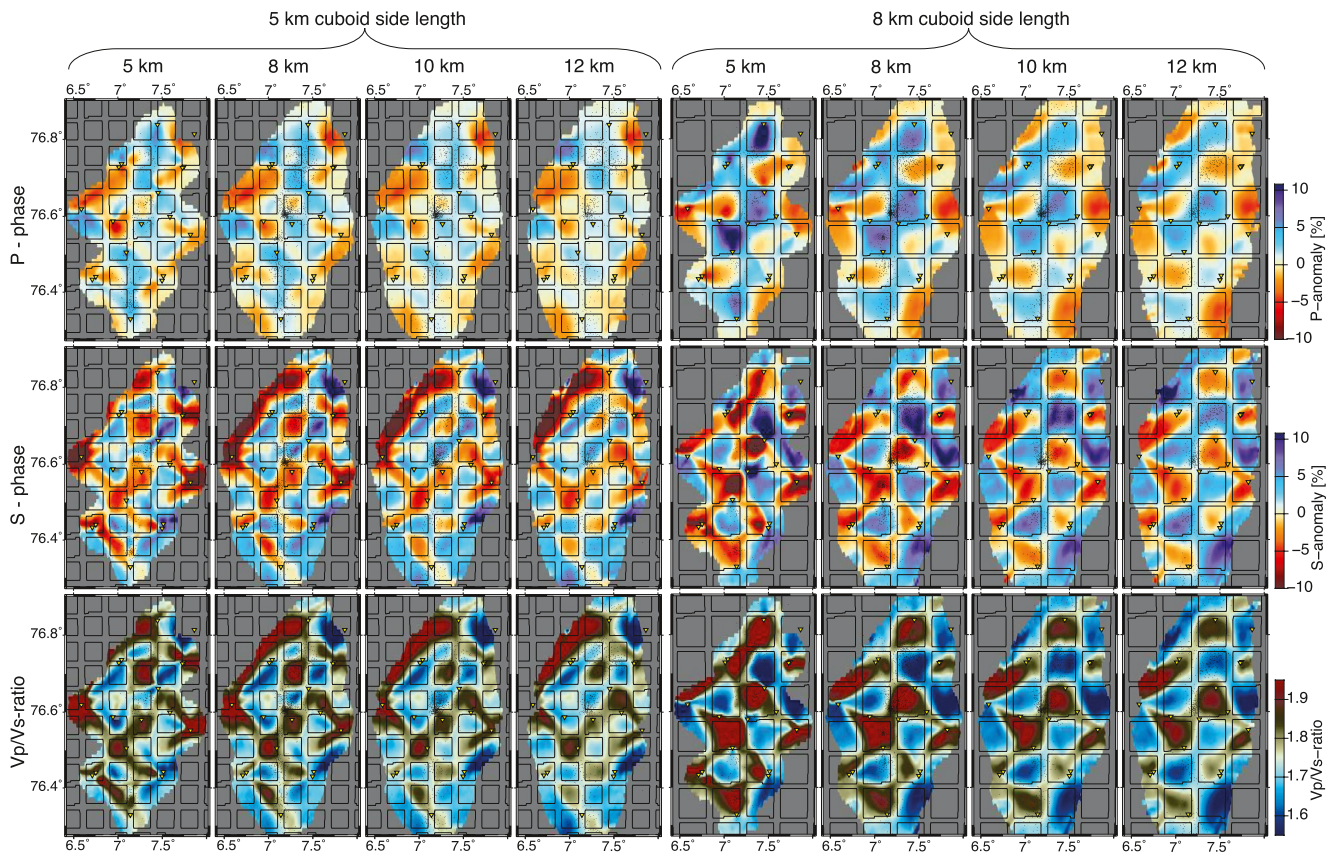
Figure 2. Checkerboard test in horizontal sections. The upper row of subfigures refers to the P-phase velocity structure, the middle row to S-phase velocity structure and the lower row to the Vp/Vs-ratio. The color code for the respective anomalies is given to the right of each row. The shapes of the checkerboard cuboids are indicated by the black lined squares. The left half of the figure represents the checkboard test with cuboids with a side length of 5 km, the right half cuboids with a side length of 8 km. Each test is subdivided into the four depth sections that are later used in results figures: 5 km, 8 km, 10 km and 12 km (below the sea level).

kilometers 25 and 35 along the profile (Figure 3), where nearly no seismicity occurs, the resolution deteriorates, but the model is still able to restore the input anomalies.

3.2.2. Synthetic Tests

Additionally, we performed synthetic tests to benchmark the tomography results. Those were carried out similarily to the checkerboard tests, but with a synthetic anomaly bounded in all three directions. The anomaly is located between 9 and 16 km depth below sea level. The P-velocity is reduced by 10% and the S-velocity is reduced by 30% compared to the surroundings. This synthetic anomaly mimics the partial melt area revealed by our real data model and has a similar lateral extent. With the same velocity reductions, the shallow partial melt area is also included in the synthetic test. The resultant velocity structure is shown in Figure 4 as map view and in Figure 5 as cross section.

The anomalies in S-velocities and in the Vp/Vs-ratio are recovered well, while the P-velocities exhibit only low amplitude anomalies, as we would expect for a partial melt area. From the synthetic test it becomes clear that especially the shallow anomalies above the large anomaly underneath the Logachev volcanic center are influenced by this deeper anomaly. Therefore, any interpretation of this shallow structure, although recovered sufficiently well in the checker board tests, has to remain speculative. Furthermore, we find that the extent of the high Vp/Vs-ratio anomaly underneath the Logachev volcanic center can not be clearly defined. A lack of seismicity at the southern boundary does not allow to define the extent of the anomaly toward the south. Similarly, the maximum depth of the anomaly remains unresolved.
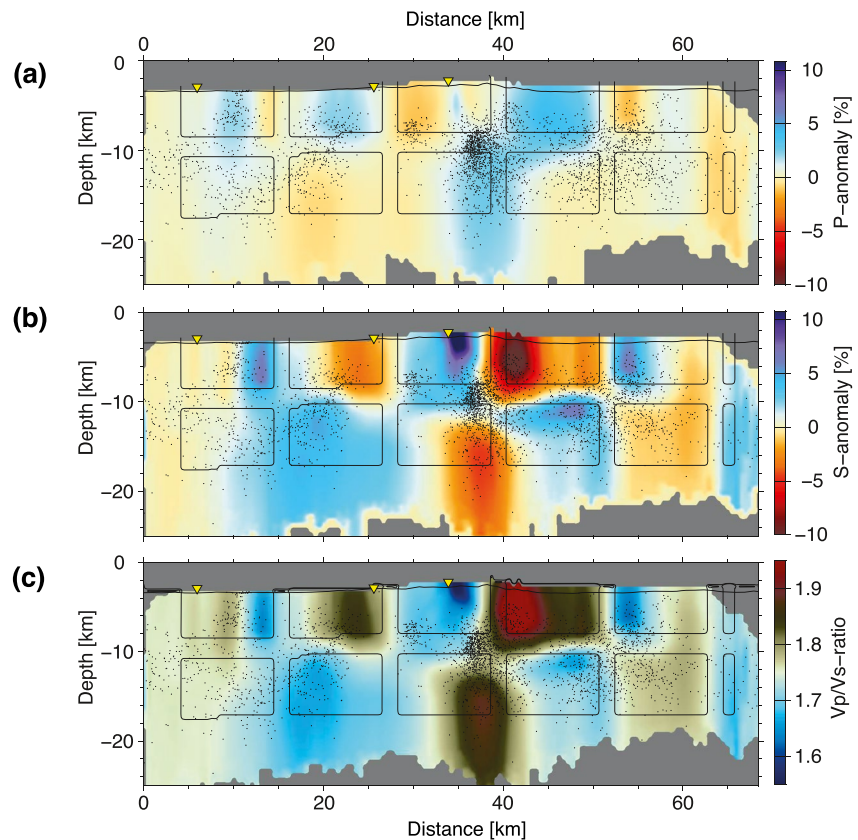
Figure 3. Checkerboard test in vertical sections. (a) Refers to the P-phase velocity structures, (b) to S-phase velocity structures and (c) to the Vp/Vs-ratio. The color code for the respective anomalies is given to the right of each subfigure. The shapes of the checkerboard cuboids are indicated by the black lined squares.

4. Results

The tomographic inversions give us insights into the subsurface velocity structure at a major volcanic center of the Knipovich Ridge in comparison with the velocity structure of the rift axis to the north and south of it. The resultant velocity structure for P- and S-waves and Vp/Vs-ratio for the Logachev area are shown in Figure 6. We focus on the P-wave and S-wave velocity structures and the Vp/Vs-ratio as they are sensitive to different parameters and thereby unravel distinct physical properties of the subsurface (Indrastuti et al., 2019).

Based on the checkerboard tests (Figures 2, 3 and Figures S1 and S2 in Supporting Information S1), synthetic tests (Figures 4 and 5) and the ray coverage (Figures S4, S5, S6 and S7 in Supporting Information S1), we distinguish between anomalies that are well recovered and therefore used for interpretation and anomalies that are poorly recovered making them unsuitable for interpretation. The interpretable anomalies are marked in the figures with letters and described in the following Section 4.1. Others are described in Section 4.2 and marked with numbers.

4.1. Key Anomaly Pattern

The P-wave velocity structure includes a very prominent low velocity anomaly (LVA) in the central part of the Logachev area, evident in map view (Figure 6, anomaly A). This anomaly spans all depth levels and sticks out from the generally higher P-wave velocities in the surrounding area. While it has a circular shape in map view in the deeper levels, it shows a more ellipsoidal shape at 5 km depth with an elongation along the rift axis. The anomaly occupies an area that is devoid of background seismicity, circular in shape and extends throughout all depth levels. Only few swarm events occur in this area. The P-wave LVA is slightly shifted southwards compared
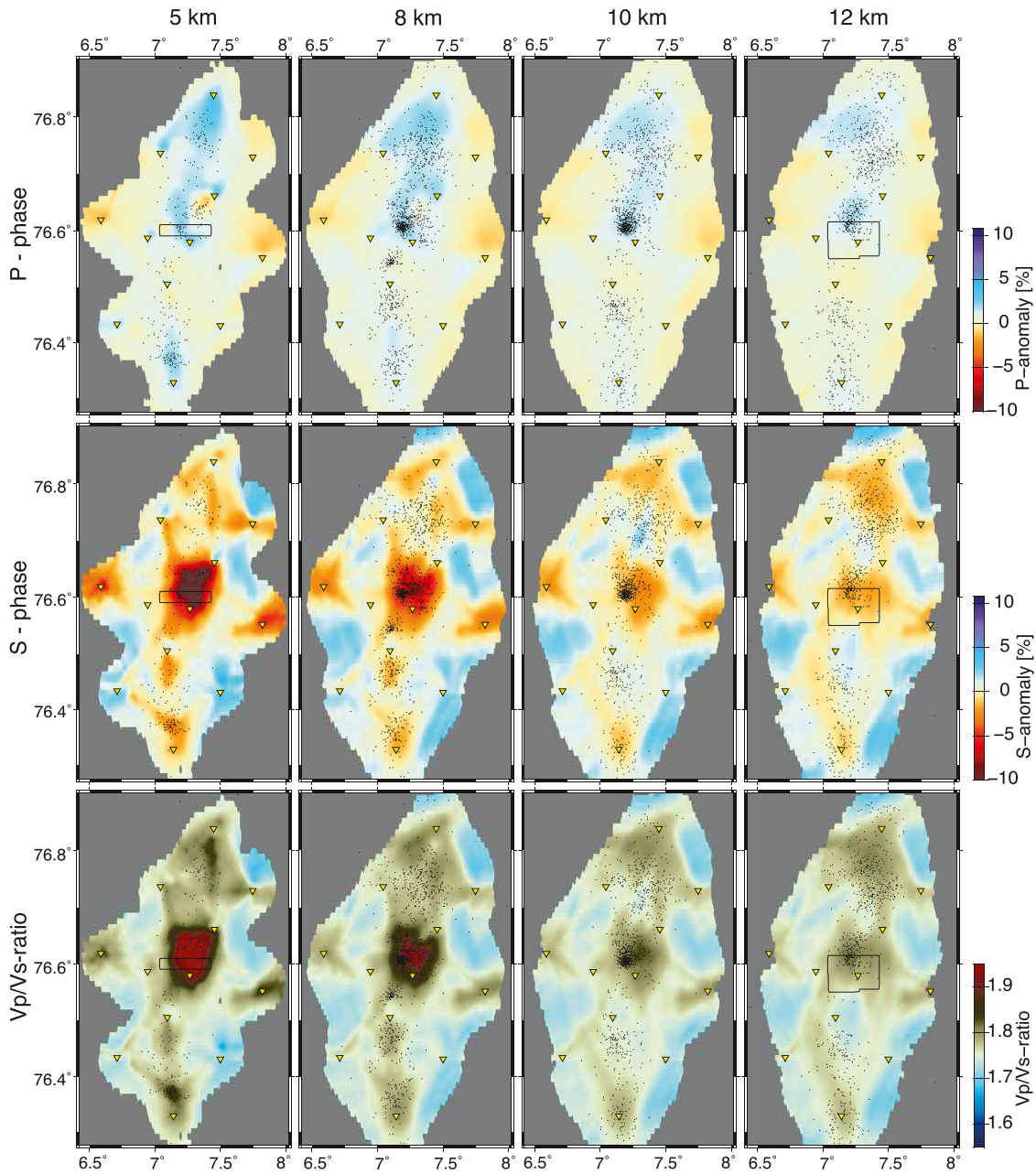
Figure 4. Synthetic test in horizontal sections. The upper row of subfigures refers to the P-phase velocity structure, the middle row to S-phase velocity structure and the lower row to the Vp/Vs-ratio. The color code for the respective anomalies is given to the right of each row. The shape of the synthetic anomalies is indicated by the black lined squares.

to the prominent anomalies in the S-wave velocity structure (anomaly B) and the Vp/Vs-ratio (anomaly C), that will be described in the following.

The S-wave velocity structure is characterized by up to 10% higher velocity deviation than the P-wave velocity anomalies, is more variable and changes with depth: at 5 km depth, several smaller LVAs occur along the rift axis. One LVA, between 76.6°N and 76.7°N (anomaly D), is about 7 km long, along the rift axis, beneath a bathymetric high with less than 3,000 m water depth. Another small LVA is found around 76.525°N (anomaly E), south of the Logachev volcanic center, whose spatial extent is roughly outlined by the 3,000 m isobath. Anomalies D and E extend down to 8 km depth, where they merge, grow in size and amplitude down to 12 km depth (anomaly
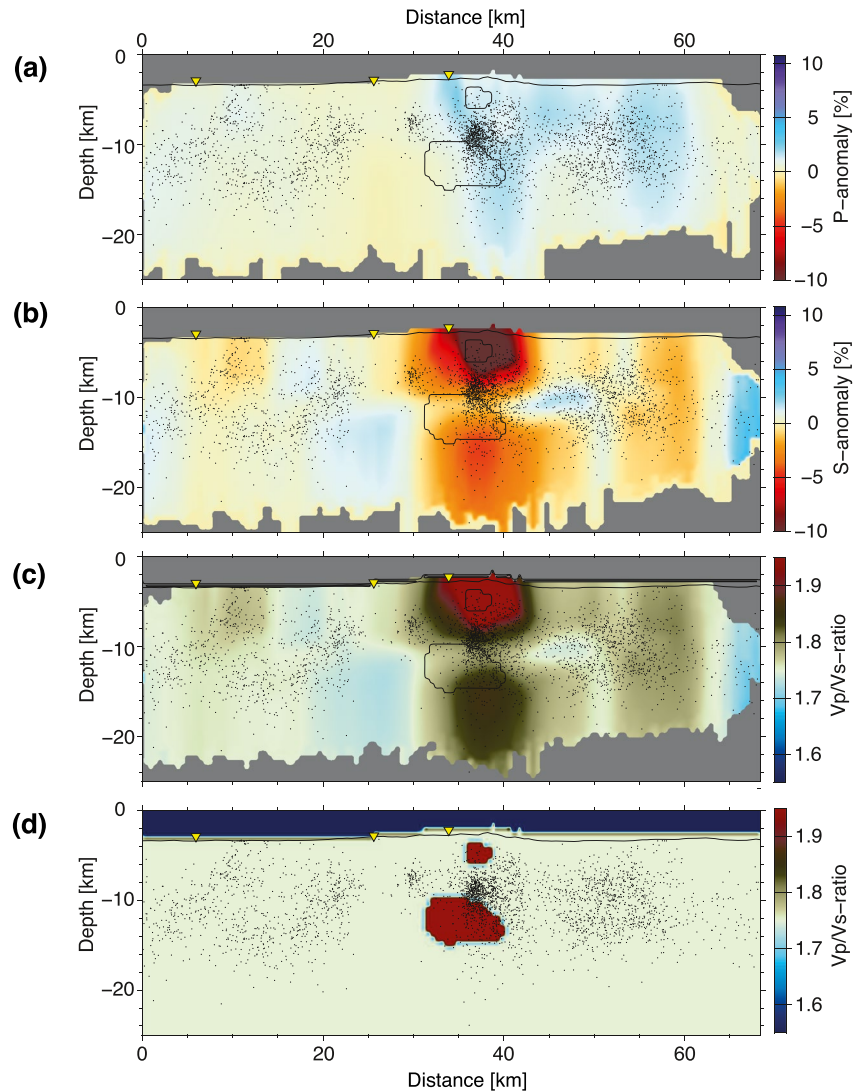
Figure 5. Synthetic test in vertical sections. (a) Refers to the P-phase velocity structures, (b) to S-phase velocity structures and (c) to the Vp/Vs-ratio. The color code for the respective anomalies is given to the right of each subfigure. The shape of the synthetic anomalies is indicated by the black lined shape.

B). Anomaly B is elongated along the rift axis, connecting northward to the shallower anomaly D. The anomaly coincides with the highest observed swarm activity (Figure 6).

The Vp/Vs-ratio is mainly influenced by variations in the S-wave velocity field. In the shallowest section (5 km depth) several small anomalies with high Vp/Vs-ratios occur. With increasing depth, these small anomalies merge into one prominent high Vp/Vs-ratio anomaly (anomaly C) underneath the bathymetric high of the Logachev volcanic center, coincident with the S-wave LVA. This anomaly appears at 10 km depth, grows with depth and reaches Vp/Vs-ratios >1.9 at 13 km. The anomaly shape in map view is a 15–20 km long ellipse beneath the spreading axis. It continues to the north, where the volcanic center ends and water depths increase again. The earthquake swarms are mainly confined to the uppermost part of the high Vp/Vs-ratio anomaly and into the base of anomaly F. Anomaly F is also confined to the rift axis for a length of around 7 km, similar to anomaly D in the S-velocity structure. To the south, a low Vp/Vs-ratio anomaly (anomaly G) has a circular shape and reaches a depth of 8 km. A high Vp/Vs-ratio anomaly (anomaly H) near 76.5°N on the eastern flank of the rift valley is mainly characterized by higher P-velocities.
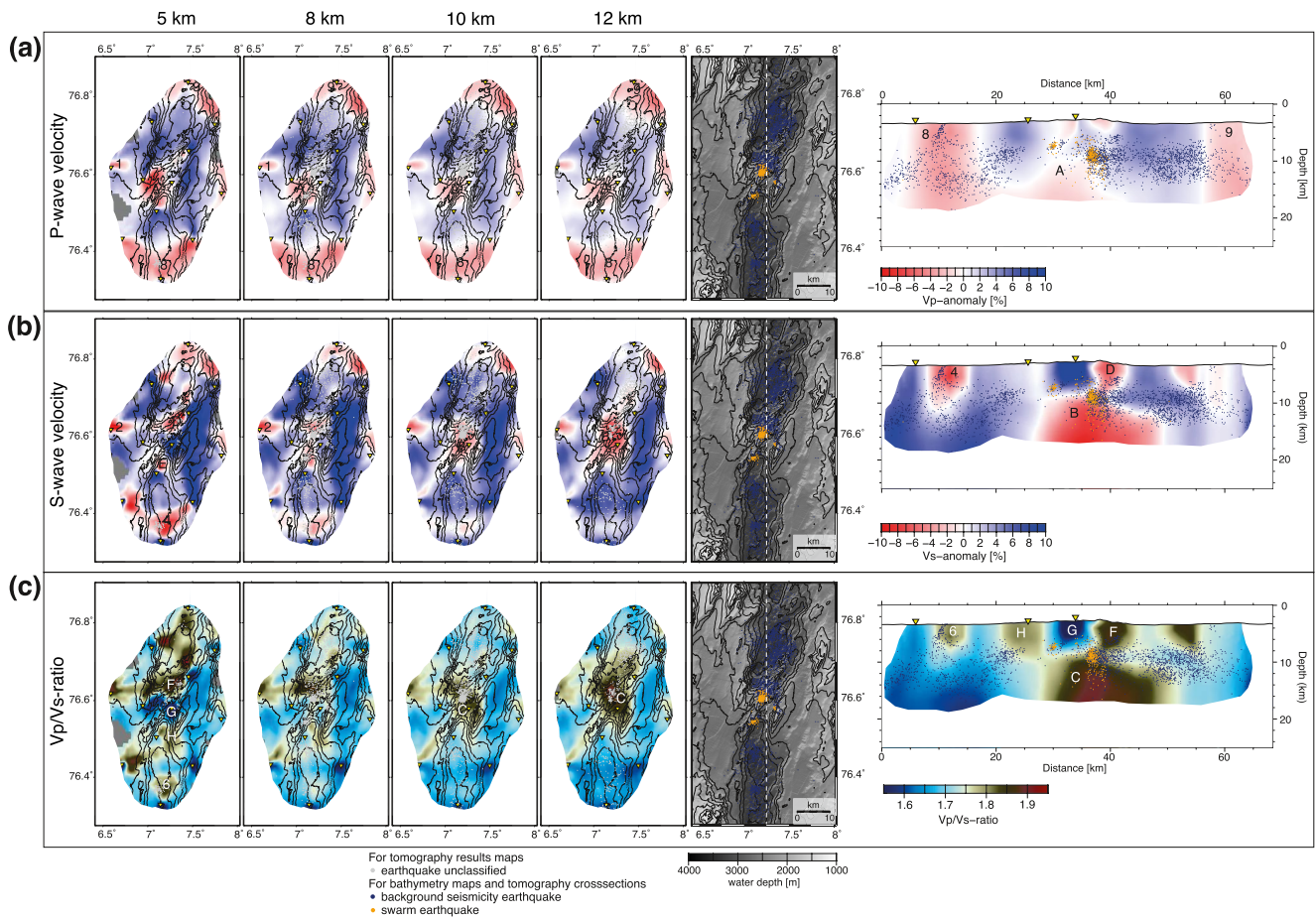
Figure 6. 3D Velocity structure of the Logachev area. Panel (a) shows the P-wave velocity structures, panel (b) the S-wave velocity structures and panel (c) the Vp/Vs-ratio. Each panel shows the map view at 5 km, 8 km, 10 km and 12 km below the sea level. The respective color code is given below the cross sections at the right side of the figure. The gray circles mark the earthquake hypocenters, yellow triangles indicate the station positions. Numbers and letters indicate anomalies that are described in the text. To the right of the map views follow bathymetric maps with color coded water depth and contour lines (thicker black solid lines are 1,000 m contours and thinner black solid lines are 200 m contours). Earthquakes are indicated with dark blue circles and swarm earthquakes with orange circles. The position of the cross section along 7.25°E is indicated with the white dashed line. The cross sections show earthquake symbols as in the bathymetric maps.

Figure 7 displays the tomography results for the entire network area on a horizontal slice at 5 km depth with P- and S-wave velocities and the Vp/Vs-ratio, results for further depths are displayed in Figure S3 in Supporting Information S1. Between 76.75°N and 76.9°N lower P-velocities occur at the rift valleys walls east and west (anomalies J). Similar to the P-wave velocities, also S-wave velocities decline between 76.7°N and 76.9°N at the rift valley walls (anomaly K). The anomalies have a similar horizontal extent as the anomalies below the Logachev volcanic center, but might be smeared due to boundary effects. S-wave velocity anomaly K does not show up prominently in the Vp/Vs-ratio. In the northern and southern part of the entire network area, we observe similar anomalies striking E-W over the entire inverted area (anomalies L and M). Another anomaly with high Vp/Vs-ratios is situated at 76.2°N (Figure 7, anomaly O), and is mainly caused by reduced S-wave velocities (Figure 7, anomaly N).

4.2. Unspecified Velocity Anomalies

Especially in the shallowest sections at 5 km depth, we observe a number of anomalies that continue in most cases only to depths of 8 km. Most of them have a small horizontal extent, which is near the lower limit of the resolution capability from the checkerboard tests. Additionally, ray coverage in 5 km depth is low (Figures S4, S5, S6 and S7 in Supporting Information S1), such that the anomalies described in this section are not used for further interpretation.
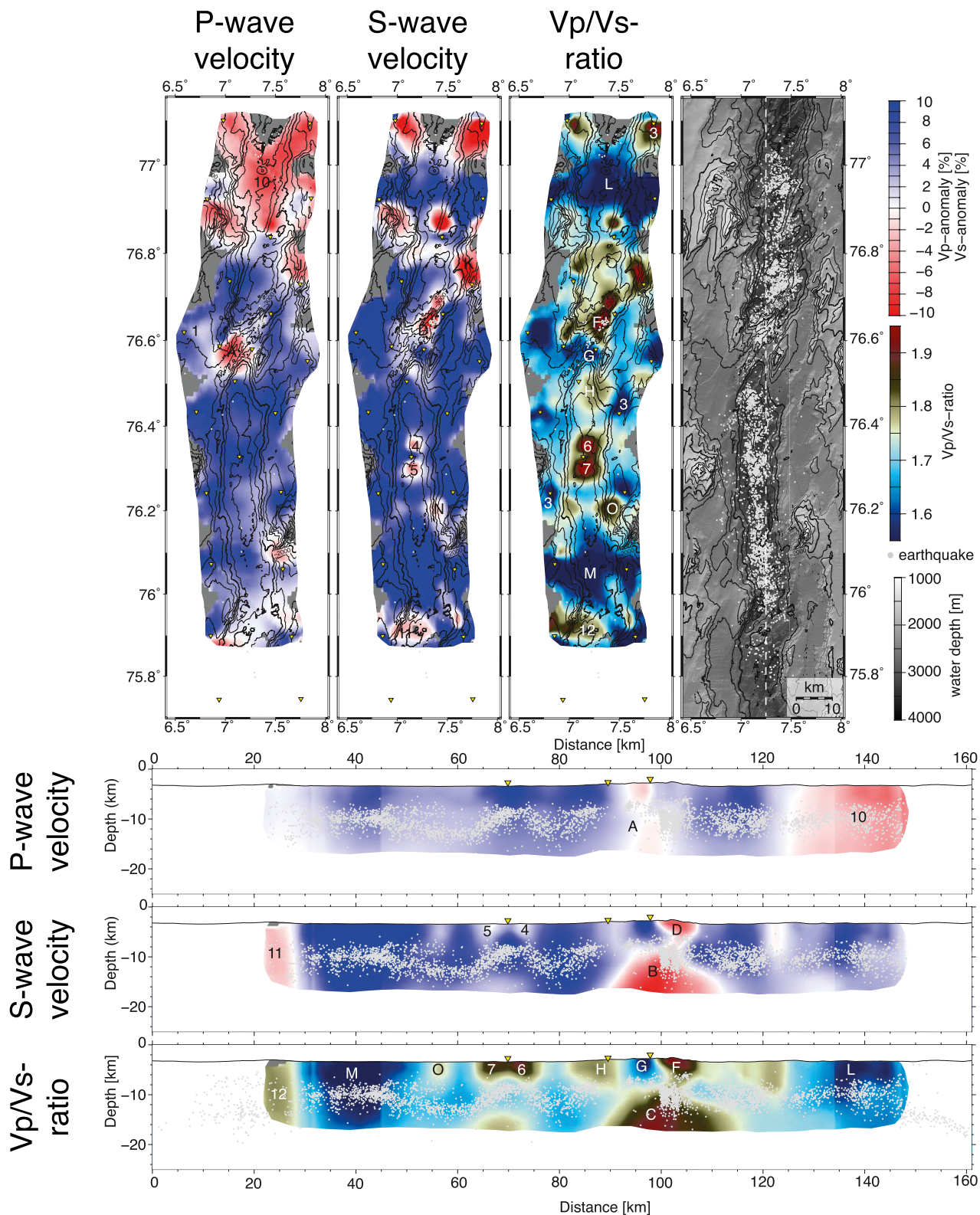
Figure 7. 3D velocity structure of the entire network area. Top: map view at 5 km below the sea level for P-, S-wave velocities and the Vp/Vs-ratio. Gray circles mark the locations of earthquakes, yellow triangles indicate the station positions. Numbers and letters indicate anomalies that are described in the text. Top right: bathymetry map with gray scale water depths (thicker black lines are 1,000 m depth contours and thinner lines 200 m contours). The position of the cross sections below is indicated with a white dashed line. The cross sections along 7.25°N show the respective velocities, Vp/Vs-ratios and earthquake locations.

Around some stations we see confined, elongated anomalies, of which the most prominent sets in at the westernmost station around 76.6°N and continues toward the east (Figure 7, anomaly 1 in P-velocities and anomaly 2 in S-velocities). This anomaly is best visible in the Logachev area, but is also present in the entire network area (Figure 6, anomaly 1). These types of anomalies, that also occur at other stations, result from a unidirectional raypath coverage, with crossing ray paths being rare or missing. This may result in velocity anomalies to be smeared along the existing ray paths and this mainly affects stations toward the edge of the network. This problem can be amended when additional ray paths are included as is the case in the center of the study area (Figures S4, S5, S6 and S7 in Supporting Information S1).

Furthermore, there are circular anomalies visible around the stations (some of them are marked as anomalies 3 in Figure 7), mainly in the shallowest section. These anomalies are most prominent in the Vp/Vs-ratio, where they, in most cases, show reduced Vp/Vs-ratios that appear as "blue holes" around the stations in Figure 7. Since these anomalies are clearly coupled to particular stations, we interpret them as a station effect, that may be explained with very localized geological conditions at the stations' positions. The OBS network consists of stations deployed along the rift flanks and some deployed within the rift valley, such that topography and geology vary significantly. Sediment thickness varies from no sediment cover at magmatically active parts to 1,500 m along the eastern flank (Curewitz et al., 2010; Kvarven et al., 2014). These geological differences cannot be accounted for in the initial 1D velocity model and therefore appear as localized anomalies in the final tomographic 3D velocity model. With large values for smoothing parameters, we could suppress this effect further, but this would at the same time reduce the resolution capability, which we tried to avoid.

We observe a high Vp/Vs-ratio north of station KNR19 resulting from low S-velocities (Figure 7, anomaly 4 and 6). This anomaly is reproduced in the entire network area and, additionally, a similar anomaly south of station KNR19 (Figure 7, anomalies 4 and 5 in S-velocity structure and anomalies 6 and 7 in Vp/Vs-ratio). The difference between the anomalies lies in the location of the corresponding earthquakes, which is probably caused by the use of different sets of phases in the respective tomographic inversion. While the entire network area includes phase readings at all stations of the network, the Logachev area only includes phase readings of stations within this confined region, although the earthquakes have been recorded by more stations outside the Logachev area. Therefore, earthquake locations near the southern limit of the Logachev area have a considerably poorer azimuthal station coverage than the same earthquakes in the entire network area. The location quality therefore is reduced toward the edges of the network and differences in the resultant velocity structure occur. The anomaly pattern recovered in the entire network area is in our opinion more reliable at the edges of the Logachev area. We therefore suggest that anomalies 4, 5, 6 and 7 are caused by these station distribution effects. Likewise, observations of a shallow earthquake cluster at a similar position by Schlindwein et al. (2013) may have also been influenced by the distribution of stations that resulted in less reliable earthquake locations with a large azimuthal gap.

The southern part of the Logachev area does not show any small-scale anomalies in the P-velocity structure, but rather large-scale regions spanning about 10 km along the cross section with low P-velocities (Figure 6, anomaly 8). Similarly, the northern end of the Logachev area also shows lower P-velocities (Figure 6, anomaly 9). These lower velocity areas are not reproduced at the scale of the entire network area. We suggest that they represent boundary effects and we will therefore not interpret them.

Boundary effects also occur at the northern and southern end of the entire network area. This results for example in low P-wave velocities in the northern part of the entire network area (Figure 7, anomaly 10) and in a high Vp/Vs-ratio anomaly close to the southern end of the entire network area (Figure 7, anomaly 12), which is dominated by low S-wave velocities (Figure 7, anomaly 11). As at the Logachev area, the resolution is reduced as a consequence of limited location accuracy (large azimuthal station gap) and limited ray coverage (Figures S6 and S7 in Supporting Information S1). Especially at the southern end, the tomographic model suffers from very few earthquakes and thereby a reduced number of ray paths. Therefore, the anomalies close to the northern and southern boundaries of the tomography model are not used for interpretation.

5. Discussion and Interpretation

5.1. Magmatic Activity at the Logachev Volcanic Center

The combined analysis of seismicity and three-dimensional anomalies in the seismic velocity structure leads to a comprehensive picture of the current magmatic activity at the Logachev volcanic center. This is shown in Figure 8 and will be described in the following. We discuss and depict the most plausible scenario based on our
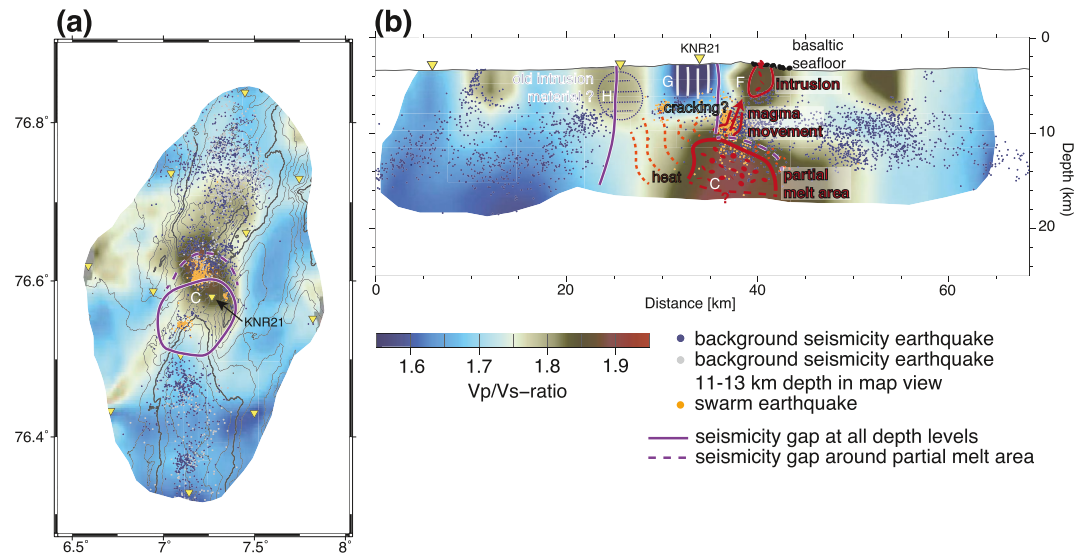
Figure 8. Interpretation of the local earthquake tomography of the Logachev area. The underlying Vp/Vs-ratio cross section is the same as in Figure 6 in the results, map view is the section at 12 km depth. Background seismicity between 11 and 13 km is gray in map view.

seismological data set. However, seismic velocities depend on a variety of physical parameters, such that in the absence of additional information the interpretation remains to some extent speculative (Indrastuti et al., 2019).

5.1.1. Melt Reservoir

The area underneath the Logachev volcanic center is underlain at a depth of 10 km by a volume of high Vp/Vs-ratios reaching maximum values >1.9. The range of expected values for melt in upper mantle rocks is between 1.8 and 2.1 (Hammond & Humphreys, 2000) with melt fractions of around 2%. Consistently, reduced S-velocities indicate the presence of fluids such as magma (Takei, 2002). We therefore suggest that there is a main melt reservoir at the Logachev volcanic center at depths of 10–12 km below sea level. The location of the this melt reservoir coincides with a mantle Bouguer anomaly low (Curewitz et al., 2010; Okino et al., 2002) and with the location of an axial high in the rift valley with elevations of about 1,000 m, which continues as a seamount chain to both sides of the rift valley (Figure 1b). Hellevang and Pedersen (2005) suggest that this seamount chain was caused by an extended period of high melt supply. While there is no general background seismicity registered, earthquake swarms root in the center of this area (Figure 8). Therefore, some extent of brittle rock failure must still be possible, suggesting that rather than a melt reservoir filled with fluids, we expect the presence of scattered melt bodies, distributed within the surrounding rocks. We therefore term this area "partial melt area".

This partial melt area may be supplied by melt focusing as suggested for ultraslow spreading ridges (Cannat et al., 2003; Schlindwein & Schmid, 2016; Standish et al., 2008). Melt is guided along the rift axis at a permeability boundary near the lithosphere–asthenosphere boundary toward the prominent, but widely spaced volcanic centers (Paquet et al., 2016; Sauter & Cannat, 2010). In our study area, melt appears to accumulate underneath the Logachev volcanic center, where the lithosphere is thinnest. Here, at the center of the segment, the melt is stored near the base of the brittle lithosphere before it rises to the surface. From the synthetic tests of our tomography model (Figures 2–5) it became clear that the lower boundary of this high-Vp/Vs anomaly cannot reliably be resolved. Therefore, we are not able to say, if this partial melt area continues further downwards and potentially extends laterally at deeper levels into the segment as a consequence of deep lateral melt flow toward the segment center.

Likewise, the synthetic tests showed that the anomaly can be recovered well especially at a depth of 12 km, but it may be smeared or shifted slightly toward the north. Above the southern boundary the most prominent earthquake swarm recorded by our OBS network took place (Figure 8b, around km 30). This earthquake swarm occurred within an otherwise aseismic area, the seismicity gap, and is distinct from the repeated swarm activity above the center of the partial melt area. The northern boundary is potentially not well resolved and smeared out, but a

further northern extent of the partial melt area as suggested by the recovered anomaly pattern would fit with the observation of Meier et al. (2021), who suggested that seismicity connected to magmatism continues rather to the north of the volcanic center than to the south. In Figure 8a this is visible from widely scattered seismicity south of Logachev volcanic center occupying a larger depth range, whereas seismicity to the north is considerably denser and concentrated in a narrower band.

5.1.2. Ongoing Magmatism and Possible Spatial Shift in Melt Supply

The partial melt area represents a volume of locally heated rocks that goes along with reduced P-velocities and a gap in seismicity (Figure 8a). The seismicity gap spans the entire depth section between km 25 and 38 along the cross section (Figure 8b) and also extends around the partial melt area, but here it exists only at deeper levels (Figure 8b). Within the seismicity gap we only observe swarm earthquakes and lack background seismicity. Higher temperatures associated with the presence of hot molten material reduce the rheological strength of the rocks in the surrounding area. Temperatures in excess of $650° \pm 100°C$ usually prevent brittle faulting (Anderson, 1995; McKenzie et al., 2005), such that an isotherm can be associated with the maximum depth of faulting. This results in a lack of earthquakes in an area surrounding the melt body. Higher temperatures also lead to lower P- and S-velocities (Indrastuti et al., 2019). The S-velocities tend to show a similar geometry and position of the anomalies as the Vp/Vs-ratio, while the main P-velocity anomaly A (Figure 6) is shifted further to the south from the Vp/Vs-anomaly. The synthetic tests in Figure 4 do not suggest that anomaly A, which is visible at several depth levels in the same location, results from poor recovery of the pronounced anomaly B. We therefore speculate that different positions of the negative P- and S-velocity anomaly may be real and result from the different sensitivity of the wave types to rock parameters. S-velocities are usually interpreted in the context of fluid content, while P-velocities also carry other information besides the presence of melt mainly the composition of rocks (Koulakov et al., 2021; Takei, 2002). We suggest, that reduced P-velocities are mainly the consequence of higher temperatures, whereas the presence of melt drastically reduces the S-wave velocities and thus results in high Vp/Vs-ratios. Therefore, we suggest that the area of both lower P- and S-velocity anomalies A and C (Figure 6) can be interpreted as an area of increased temperatures since it also coincides with the seismicity gap. Partial melt, however, is only present in the area of the Vp/Vs anomaly C. In case the southern end of anomaly C is not well retrieved and shifted to the north, the entire area may contain some partial melt.

We suggest that melt rises to the surface from the partial melt area. The high, nearly monthly, earthquake swarm activity (Meier et al., 2021) connects the partial melt area and the shallow high Vp/Vs-ratio anomaly F (Figure 8). Even with limited resolution of this area, we can speculate that the high Vp/Vs-ratios and lower S-velocities image the presence of melt also in this shallow area, in analogy to the deeper partial melt area. This interpretation is supported by the earthquake activity and geological samples. Fresh basalt samples from the seafloor (Elkins et al., 2014) indicate that recent volcanic activity occurs here. The earthquake swarms potentially indicate the path of the melt flow from the center of the lower partial melt area to the shallow reservoir. The swarms occur always at a similar position and repeat regularly (Meier et al., 2021) suggesting steady melt supply upwards. The site of current activity of the Logachev volcanic center seems to be stable during our observation period. Plotted over time, the individual earthquake swarms, even when relatively located, do not exhibit a clear migration of hypocenters (Meier et al., 2021), which would indicate a cracking front of a magma intrusion (Bohnenstiehl et al., 2008). Despite a lack of clearly migrating hypocenters, the earthquake swarms are the only seismic activity in an otherwise aseismic area underneath a volcanic center (Figure 8b). The absence of migration could be due to the reuse of already existing pathways that make the breaking of completely new pathways unnecessary. The melt pathways all trend slightly to the north to the area with fresh basalt on the seafloor (Figure 8b). Tarasewicz et al. (2012) note very similar earthquake clusters without migration and distinctly different positions at similar depth intervals preceding the flank eruption at Fimmvörðuháls on Eyjafjallajökull, Iceland. They interpret this seismic activity to indicate magma movement in several dikes.

The region of magmatic activity shifts over time (Figure 9). South of the partial melt area, the velocity structure can not be resolved (Figures 4 and 5), such that we do not know if the partial melt area continues further south. But we clearly see the absence of background seismicity, that we interpret to be caused by elevated temperatures in the south of the partial melt area. This may be a remnant of previous activity in this area that is still heated up, while magmatic activity has shifted northward. From the current, central partial melt area intrusions tend northwards into an area that still exhibits background seismicity. We speculate that this area is not yet heated up
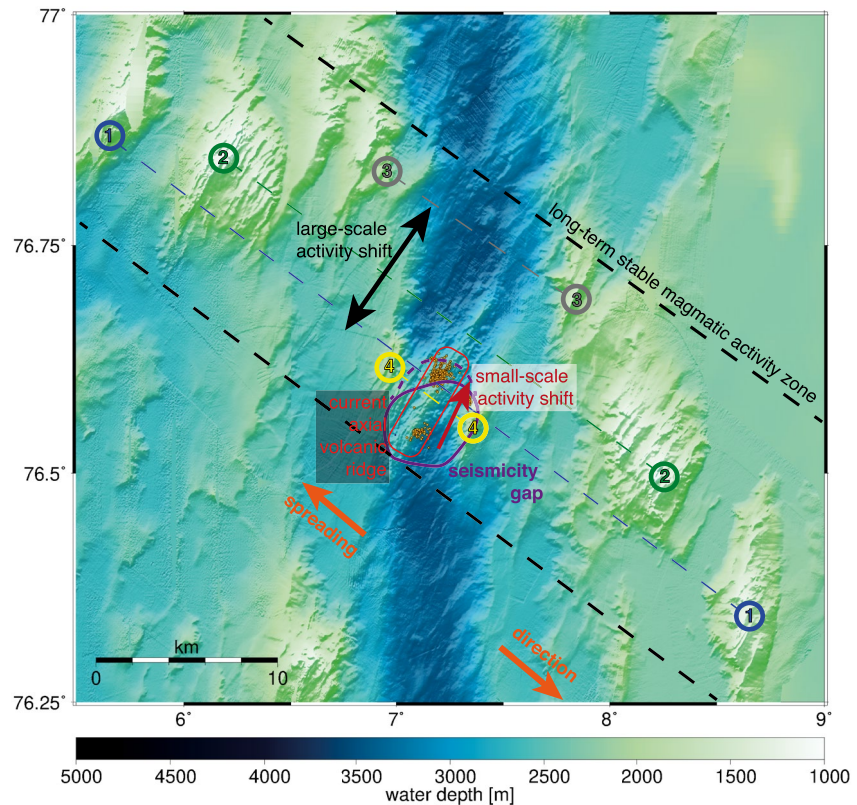
Figure 9. Activity shift on different scales at the Logachev volcanic center. The black dashed line marks the long-term stable magmatic activity zone as described by Hellevang and Pedersen (2005). The bathymetry in spreading direction (orange arrows) from the Logachev volcanic center shows several pairs of elevated volcanic hummocks marked with colored circles and numbers according to evolution stage (1 corresponds to the oldest pair of elevated volcanic hummocks indicated here). Colored dashed lines connect the pairs and mark the position of magmatic activity in the rift valley during their development. The large-scale activity shift inferred from them is marked with the black arrow. The small-scale shift indicated by our data set with the seismicity gap (purple) and earthquake swarm activity (orange circles) is shown with the dark red arrow, while the red box marks the currently active axial volcanic ridge.

sufficiently to prevent brittle failure and hence became only recently volcanically active. Mapping of volcanic seafloor off-axis at ultraslow spreading ridges suggests that activity varies between phases of magmatism and tectonism (Mendel et al., 2003). The history of activity shifts is also indicated by the off-axis bathymetry in spreading direction from the Logachev volcanic center as individual volcanic edifices (Figure 9). In general, the activity stays in the same region and was stable for the last 7–8 Ma (Hellevang & Pedersen, 2005), but cycles of magmatic and tectonic activity at the Southwest Indian Ridge last about 0.4 Ma (Mendel et al., 2003). At Logachev volcanic center, the youngest high-elevation ridges of the seamount chain are considerably offset to the north compared to the current position, whereas older ridges are positioned in spreading direction from the current axial volcanic ridge (Figure 7). This gives an impression of the different scale of spatial and temporal shifting of the magmatic activity. The shift of activity indicated in our study occurs on a smaller scale of few kilometers within the current volcanic edifice of the Logachev volcanic center itself compared to the large-scale activity shift that built the individual volcanic edifices. Hence, we suggest that we observe a more small-scale shift within one volcanic center within a typical cycle of activity.

5.1.3. Shallow Crustal Structure of the Logachev Volcanic Center

The synthetic test (Figures 4 and 5) showe that the resolution capability of our tomography model is reduced in the shallower part of the Logachev volcanic center, such that the following interpretations remain speculative and require validation by additional data sets. The resolution in this part of our model suffers from reduced ray coverage due to a lack of earthquakes in the seismicity gap (Figures S4, S5, S6 and S7 in Supporting Information S1).

The synthetic test in Figure 5 suggests that the high Vp/Vs-ratio of anomaly H is not a result of imperfect recovery of anomaly B, but represents a real feature. We therefore tentatively interpret anomaly H (Figure 8) as remnants of older intrusions that could exist above the area of higher temperatures south of the partial melt area (anomaly H in Figure 8). The high Vp/Vs-ratio is caused by slightly elevated P-wave velocities of 4.5–6 km/s (Figures S8 and S9 in Supporting Information S1), while the S-wave velocities do not indicate a clear deviation from the initial velocity model. Increased P-wave velocities in volcanic regions are usually interpreted as older and now cooled intrusions (Greenfield et al., 2016; Schuler et al., 2015). P-wave velocities are sensitive to changes in the lithology (Christensen, 1996), expecting higher velocities of around 7 km/s and Vp/Vs-ratio of more than 1.8 for gabbro and lower velocities with around 6 km/s for basalt (Christensen, 1996). In the Askja Caldera in Iceland, Greenfield et al. (2016) detected an area with low P-wave velocity and interpreted this as an older basaltic intrusion. Our absolute velocities rather indicate basalt, while the Vp/Vs-ratio indicates gabbroic rocks, but factors such as porosity can also affect velocity (Christensen, 1996). Hence, we can only speculate on the presence of older intrusions with possible changes in lithology here.

To the north of this area and underneath station KNR21 (Figure 8) we observe a very low Vp/Vs-ratio anomaly G. The synthetic test (Figure 5) rather predicts a positive Vp/Vs-ratio anomaly at this location as an artifact of the deep anomaly B, so we tentatively interpret negative anomaly G as being potentially real. We speculate that it may show characteristics of a highly cracked area. A study by Curewitz et al. (2010) revealed in general fewer, but longer faults at volcanically active regions along the Knipovich Ridge. The low Vp/Vs-ratio is mainly defined by high S-velocities in this area above 3 km/s, while the P-velocities only show slightly lower, mainly intermediate velocities between 4 and 5 km/s (Figures S8 and S9 in Supporting Information S1). The anomaly is situated directly underneath station KNR21. Very low Vp/Vs-ratios of 1.5 together with low P-velocities of 4–5 km/s and no or positive S-anomalies in magmatic contexts are interpreted by Koulakov et al. (2020) as gas-saturated rocks, possibly as part of hydrothermal systems. Schuler et al. (2015) interpreted low Vp/Vs-ratios in the Icelandic Krafla caldera as caused by high porosity and crack density in combination with the presence of steam. Along the Juan de Fuca Ridge low Vp/Vs-ratio with both low P- and S-velocities are interpreted as the upflow zone of a hydrothermal system with large cracks (Kim et al., 2019). The anomalies' location above the inferred partial melt area would be reasonable for volatiles rising from the partial melt area to the surface. Hydrothermal activity is unexpectedly high along ultraslow spreading ridges (German et al., 1998) and was already observed at the southern Knipovich Ridge (Connelly et al., 2007). In the area of our low Vp/Vs-ratio anomaly, Tamaki et al. (2001) observed a plume in the water column, but were not able to identify its source at the seafloor. A hydrothermal system would be a plausible source for the velocity anomalies. On the other hand, the S-velocities are reduced to about 10% from the initial velocity model. This is more than the around 3% deviation in the P-velocities (Figure 6), in contrast to the observations described by Koulakov et al. (2020). Additionally, a hydrothermal system in the vicinity of an OBS station could produce distinctive signals in the seismic record, for example, tremor signals, as observed at the Southwest Indian Ridge (Meier & Schlindwein, 2018). The tremor signals that we observe at the Knipovich Ridge were mainly associated with bottom currents interacting with the OBS stations (Essing et al., 2021). Therefore, we are missing a solid evidence for active hydrothermal activity in this area. However, station KNR21 showed an abundance of short-duration events (SDE) also recorded by OBS placed near other hydrothermal systems (Liu et al., 2019; Sohn et al., 1995). Another explanation for a lowered Vp/Vs-ratio would be increased crack density, which also reduces the P-velocity stronger than the S-velocity, as seen in the P- and S-velocity structures close to the surface between kilometers 20 and 27 along the profile (Figure 6). With an increase in crack density and active cracking, we would also expect an increased seismicity in the area, but this is missing here. However, in the seismic record of station KNR21 directly above this region, we observed a high number of very small earthquakes that were not recorded by other surrounding stations and hence could not be located with our location procedure (Meier et al., 2021). Therefore, we suggest that an area with a high crack density is found here, but the cracks are very small and do not produce seismicity at magnitudes that we can locate with our network. For this area close to the venue of current magmatic activity, changes in the stress field are reasonable (Buck et al., 2006). Whether the cracks additionally host active hydrothermal circulation cannot be concluded from our data set.

5.2. Volcanic Centers at Ultraslow Spreading Ridges

Local earthquake tomography studies at ultraslow spreading ridges are rare due to the high logistic effort in accessing these remote ridges. Schmid et al. (2017) conducted a local earthquake tomography study at the Segment-8 volcano at the Southwest Indian Ridge, which we compare to our results in Figure 10. The tomography results
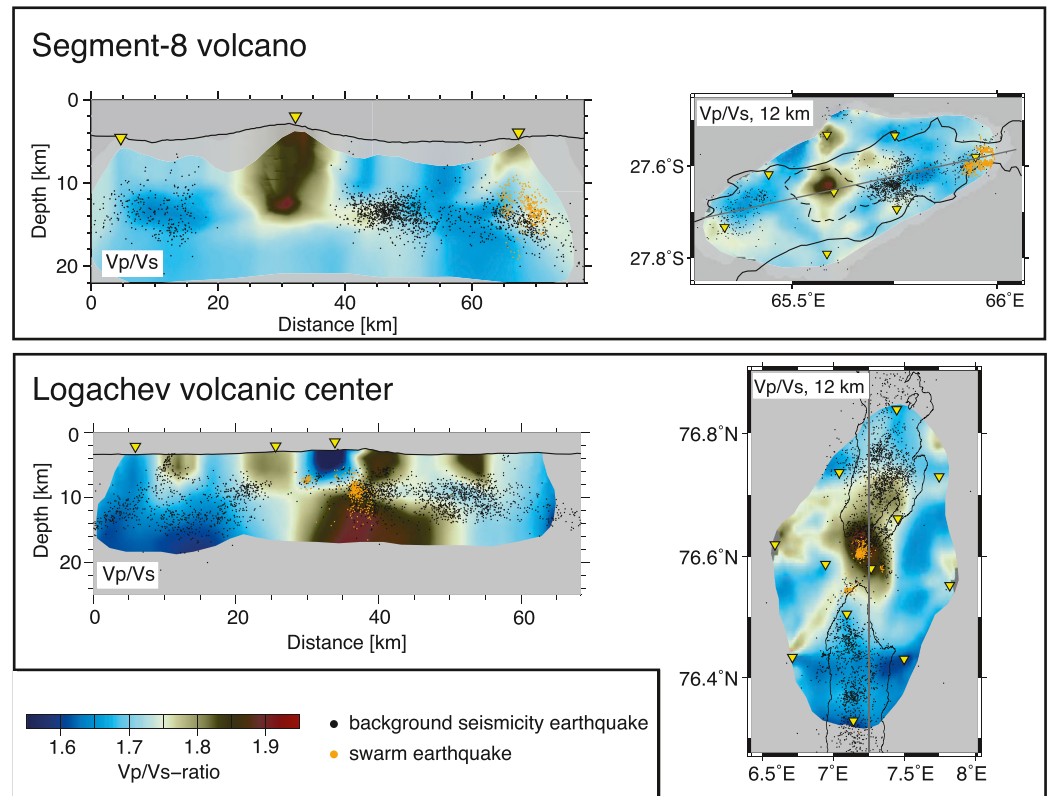
Figure 10. Vp/Vs-ratio of the Segment-8 volcano (upper row) and the Logachev area (lower row). Earthquakes are marked as black circles, swarm earthquakes as orange circles, yellow triangles mark the station positions. The position of the cross section is indicated by the gray line in the map view. The black lines display the rift valley boundaries. At the Segment-8 volcano the dashed line marks the volcanic edifice.

from the Segment-8 and Logachev volcanoes share three key characteristics, which seem to be a common feature of volcanic centers at ultraslow spreading ridges: (a) a spatially confined more or less circular area of partial melt at depths of around 10–12 km below sea level, 7–9 km below the seafloor respectively, (b) a prominent area without seismicity surrounding this anomaly and (c) intense earthquake swarm activity pointing to ongoing magmatism. The circular partial melt areas extend for about 5–15 km along the rift axis, whereas the area devoid of seismicity is in both areas around 15–20 km in diameter.

The differences appear in the detailed view of the anomaly pattern. The partial melt area at the Segment-8 volcano with around 5 km diameter is smaller than at the Logachev volcanic center. The different sizes of partial melt areas (5–10 km at the Segment-8 volcano and 10–15 km at the Logachev volcanic center) might be either due to a different structure of the ridges or a different time stage in an eruptive cycle.

The Segment-8 is spreading orthogonally. Orthogonal spreading allows magma feeding into adjacent subordinate segments. This feeding process at shallow depths is found from geological mapping in other locations of the Southwest Indian Ridge (Sauter et al., 2001, 2002). At the Segment-8 volcano, Schmid et al. (2017) and Meier and Schlindwein (2018) showed that the neighboring subordinate Segment 7 is contemporaneously magmatically active and potentially fed over 35 km along axis by a larger melt accumulation underneath the Segment-8 volcano (Schmid et al., 2017). In contrast, the Knipovich Ridge is very obliquely spreading (Curewitz et al., 2010). Therefore, the length of individual spreading subsegments is limited as they run into the rift bounding walls and lateral feeding over distances of 35 km, comparable to the orthogonal spreading Segment-8, to the next subordinate segment is not possible. Based on the seismicity pattern, Meier et al. (2021) defined subsegments separated by small transfer faults, that may prevent lateral feeding of melt at shallower depths. So, more melt might accumulate in the central partial melt area and cannot easily be redistributed in a larger area. The location of swarm activity supports a scenario, in which melt rises to the surface above the

partial melt area and no shallow horizontal magma feeding takes place over larger distances. From the partial melt area, the earthquake swarms map the current intrusion activity within 5 km along axis directly above the partial melt area and within the seismicity gap at the Logachev volcanic center. Earthquake swarm activity happens regularly with nearly one swarm per month (Meier et al., 2021), but a migration of hypocenters is not obvious. The swarm activity rather occurs associated with diking than along tectonic fault zones. In the absence of fault plane solutions (Meier et al., 2021) we can not distinguish if the earthquakes are directly or indirectly (e.g., by fracturing around the dike tip) caused by the magma movement. Earthquake swarm activity indicates that melt rises in an already existing and established intrusion zone, where the complete breaking of a path is not necessary. Background seismicity is absent because of enhanced temperatures and therefore we are not able to seismically trace faults that are speculated to serve as melt pathways (Montési et al., 2011; Standish et al., 2008). In contrast, at the Segment-8 volcano, only three swarm events were observed during the 10-month observation period. These swarms showed a clear migration (Meier & Schlindwein, 2018) and occurred away from the melt zone underneath the Segment-7. We assume that they are associated intrusions into a colder and more brittle area without earlier established pathways.

In both areas, denser background seismicity between the volcanic center and the intrusion position is potentially an effect of magmatism. The background seismicity is increased on the northern side of the Logachev volcanic center beyond the current intrusion activity, but above and adjacent to the partial melt area (Figure 10), and similarly on the eastern side of the Segment-8 volcano toward the contemporaneously active Segment-7 volcano. The interplay of tectonism and magmatism would favor individual faults as pathways for melt as described by Standish et al. (2008). Even in relative location, the earthquakes do not trace individual fault planes, such that we speculate that the enhanced background seismicity resembles a diffuse response of the local stress field on the intrusion activity (Dahm, 2000).

The position of magmatic activity along an ultraslow spreading ridge can change over different temporal and spatial scales. Periods of magmatic activity and volcanism may last for years to decades (Schmid et al., 2017). Along the Gakkel and Southwest Indian Ridges, the beginning of such an activity phase is found to be accompanied by teleseismically recorded earthquake swarms with magnitudes up to Mw 5.0 (Müller & Jokat, 2011; Schlindwein, 2012; Tolstoy et al., 2001). Along the Knipovich Ridge no earlier comparable teleseismic swarm activity was observed. If teleseismic swarms mark the beginning of activity phases, we cannot define for how long the Logachev volcanic center is in its currently active phase. But, from an 10-day long OBS study in 2009 (Schlindwein et al., 2013), we know that the seismicity gap existed already 8 years ago at the same location. At the Segment-8 volcano in contrast, intense swarm activity preceded the local earthquake tomography study by more than 16 years. At Gakkel Ridge, a local earthquake tomography conducted 8 years after the onset of the largest mid-ocean ridge earthquake swarm observed (Schlindwein, 2012), showed no clear evidence for either a seismic gap or a comparable shallow partial melt reservoir (Korger & Schlindwein, 2014). Hence partial melt reservoirs may be short-lived features in a volcanic cycle and their volume extent may be, amongst others, a function of time within a cycle.

In comparison to fast spreading ridges, volcanic centers at ultraslow and slow spreading ridges show a deep melt reservoir that is spatially confined underneath volcanic centers of the rift axis. The extent of magma chambers, melt lenses or partial melt areas greatly depend on the spreading velocity (Dunn & Forsyth, 2007). While the top of the partial melt areas at ultraslow spreading ridges appear to be as deep as 10 km, at the fast spreading East Pacific Rise Dunn et al. (2000) observed in a refraction tomography study low P-wave velocity anomalies at 2–4 km depth underneath the rift axis seafloor. These anomalies were interpreted as a continuous partial melt area extending along the ridge. Similarly, Toomey et al. (2007) find continuous low P-wave velocities along 230 km of the rift axis interpreted as a mush zone. At the slow spreading Mid-Atlantic Ridge Singh et al. (2006) and Combier et al. (2015) detected a magma chamber at 5 km depth. Here, the magma chamber extends only around 7 km along the rift axis (Singh et al., 2006). Therefore, partial melt areas at slow spreading ridges appear to be similarly confined in along-axis extent as on ultraslow spreading ridges (Dunn et al., 2005, 2017). Lower melt supply at ultraslow spreading ridges compared to slow spreading ridges might result in generally smaller melt reservoirs, but the melt focusing process at ultraslow spreading ridges might be able to accumulate larger partial melt areas. Our results indicate that these melt reservoirs occur at greater depths compared to slow spreading ridges, most likely because of the thicker brittle lithosphere at ultraslow spreading ridges (Standish et al., 2008). Local earthquake tomography studies and refraction seismic studies are still too sparse to establish whether

partial melt areas are more densely spaced along slow spreading ridges than ultraslow spreading ridges or exist more frequently in time.

5.3. Other Volcanic Centers at the Knipovich Ridge

The tomography model of the entire network area reveals the large-scale velocity structure around the Logachev volcanic center and adjacent smaller volcanic centers. It therefore allows to address the question whether any of the other volcanic centers is comparatively active.

Higher Vp/Vs-ratios around the volcanic center between lower Vp/Vs-ratios to the north and south indicate a general change in the lithospheric structure from the volcanic centers to interbedded areas that are devoid of active axial volcanic ridges (Figure 7). This underlines the assumption by Meier et al. (2021) based on the seismicity analysis that the area between 76.3°N and 76.93°N is mainly characterized by magmatic activity. At the intermediate spreading Juan de Fuca Ridge symmetric patterns of alternating high and low velocity variations are observed at shallow depths parallel to the rift axis (Barclay & Wilcock, 2004; Weekly et al., 2014). We do not observe similar patterns, but rather individual and circular velocity anomalies.

Individual anomalies of higher Vp/Vs-ratios (anomaly O; Figure 7) or lower P- and S-velocity anomalies (anomalies J, K and N; Figure 7) may give hints on former sites of magmatic activity. The anomalies occur in combination with elevated areas at the rift flanks, where off-axis seamount chains indicate that enhanced melt supply was present in the past (Curewitz et al., 2010). As discussed above in Section 5.1.2, magmatic activity can change its position along ultraslow spreading ridges and thereby builds individual seamounts over time (Mendel et al., 2003). From the seismicity however, we have no indications that active magmatism is currently taking place at these locations. We neither observe a gap in seismicity, nor earthquake swarm activity. Without indications for recent activity within the rift valley, we suggest that velocity anomalies result from older intruded material that is possibly cracked.

Underneath a second volcanic center at 75.9°N we find weak indications for the presence of melt. This volcanic center has, amongst others along the Knipovich Ridge been defined by morphology, gravity and magnetic characteristics (Curewitz et al., 2010; Okino et al., 2002). The volcanic center at 75.9°N is additionally found to continue as a seamount chain in spreading direction indicating long-lasting magmatic activity (Curewitz et al., 2010). In our study area we cover two robust volcanic centers, the major Logachev volcanic center and a second one around 75.9°N (Curewitz et al., 2010). The bathymetry map (Figure 1) shows a prominent circular cone that we suggest to be of volcanic origin like similar features at the Gakkel Ridge 85°E volcanic center (Pontbriand et al., 2012). Underneath this cone and to the western flank we observe higher Vp/Vs-ratios (anomaly 12; Figure 7) and lower S-velocities (anomaly 11; Figure 7). This could indicate a melt volume underneath this second volcanic center, but as discussed earlier, the resolution of the tomographic model at the boundaries of the inverted area is insufficient and the observed anomaly could also be an artifact.

In the areas between volcanic centers or paired seamount chains, low Vp/Vs-ratios, caused by high S-wave velocities, cover the rift valley in full width. These areas coincide with earthquakes reaching down to depths of 15 km. We suggest that these areas are not characterized by volcanism, but rather have older and cooled rocks possibly from gabbroic intrusions of higher seismic velocities (for P-waves of 7.5–8 km/s and for S-waves of 4.5–5 km/s) and a thickened brittle lithosphere. P-wave velocities of around 7 km/s are associated with gabbroic rocks (Christensen, 1996). With increasing depths, the low Vp/Vs-ratio in the North (anomaly L; Figure 7) reduces and Vp/Vs-ratios increase in the rift valley again, whereas the southern anomaly M exhibits low Vp/Vs-ratios throughout all depth levels also in the rift valley. The southern part of the study area is inferred to be influenced by the reorientation of the ridge (Curewitz et al., 2010; Meier et al., 2021). Probably the more tectonic character of the area also has an influence on the velocity structure compared to the northern part.

The lower velocities at the northern end of our study area (anomaly 10) correspond to lower velocities that are detected in full waveform inversion (Rickers et al., 2013) and in delays of phase arrivals at OBS stations positioned to the west of the ridge axis (Jeddi et al., 2021). These studies resolve the velocity structure at greater depths than we do, but may both point to an area with different lithospheric architecture and properties, such as elevated temperatures or different composition.

6. Conclusions

From the local earthquake tomography study along the Knipovich Ridge we gain insights into the magma plumbing system at its Logachev volcanic center and at ultraslow spreading ridges in general.

1. Lower S-velocities and higher Vp/Vs-ratios indicate a partial melt area underneath the Logachev volcanic center at a depth of 10 km below the sea level. Here, the melt accumulates through processes of melt focusing before ascending to the surface.
2. The ascending melt from the partial melt area is associated by high earthquake swarm activity. Densely clustered earthquake swarms root in the center of the partial melt area and connect this area to a shallow intrusion area as evidenced from high Vp/Vs-ratios. This area lies slightly to the north of the deep partial melt area. In a zone surrounding the partial melt area heat prevents brittle failure of rocks and a seismicity gap is observed. This warm area extends further south than the current swarm activity. From this spatial offset we infer a small-scale shift of the magmatic activity toward the north.
3. Velocity structures in the shallow crust show some indications for older intrusions and an area with a high density of cracks next to it. Although likely, we are not able to find in our data set clear indications of hydrothermal circulation in the cracked area.
4. Partial melt areas underneath major volcanic centers of ultraslow spreading ridges have nearly circular shape and occur in depths of 10–12 km below sea level (7–9 km below the seafloor). Magmatic activity underlies a cyclic variation. Initiation of an activity phase typically coincides with high teleseismic earthquake swarm activity marking the preparation of pathways for melt intrusion. We postulate that the Logachev volcanic center is currently in a phase of established magmatism, where earthquake swarms do not show the breaking of new pathways, but rather movement of magma in existing paths. Feeding processes to subordinate volcanic centers, as seen at the Southwest Indian Ridge Segment-8 volcano over distances of 35 km, are prevented by the obliquity of the ridge. Lateral feeding only occurs within the axial volcanic ridge area over short distances of 5 km.
5. In the velocity structure of the Knipovich Ridge at segment scale, we can identify anomalies coinciding with elevations in the axial morphology probably marking areas of former magmatic activity. The second major volcanic center of our study area shows high Vp/Vs-ratios underneath a volcanic cone in the rift valley, but restricted resolution of our tomography model near the edges of the seismic network forbids any conclusion on the presence or absence of melt bodies.

Our study shows that the passive seismic studies that explore the seismicity of ultraslow spreading ridges can shed light on the interplay of tectonism and magmatism in spreading processes. In addition, the local seismicity provides an excellent source for seismic rays used in local earthquake tomography to image the upper lithosphere. We are able to image the magma plumbing system of an active volcanic center and the underlying system of melt ascent. Local earthquake tomography studies at mid-ocean ridges are still rare, but especially at slow spreading rates with intensive and deep reaching seismicity they constitute a valuable tool for imaging lithospheric structure beyond the depths of active source seismology.

Data Availability Statement

The used algorithm for local earthquake tomography is available (Koulakov, I.; LOTOS, code for non-linear local earthquake tomographic inversion; https://www.ivan-art.com/science/LOTOS/index.html; Version 12). The bathymetric raw data (Bohrmann & dos Santos Ferreira, 2018; Bohrmann & Wintersteller, 2018; Damm et al., 2018; Schlindwein & Wölfl, 2018), the seismicity raw data (Schlindwein et al., 2018), the earthquake catalogue (Meier et al., 2020) and phase picks (Meier & Schlindwein, 2022) are published.

References

Amundsen, I. M. H., Blinova, M., Hjelstuen, B. O., Mjelde, R., & Haflidason, H. (2011). The Cenozoic Western Svalbard margin: Sediment geometry and sedimentary processes in an area of ultraslow oceanic spreading. *Marine Geophysical Research*, *32*(4), 441–453. https://doi.org/10.1007/s11001-011-9127-z

Anderson, D. L. (1995). Lithosphere, asthenosphere, and perisphere. *Reviews of Geophysics*, *33*(1), 125–149. https://doi.org/10.1029/94RG02785

Barclay, A. H., & Wilcock, W. S. D. (2004). Upper crustal seismic velocity structure and microearthquake depths at the endeavour segment, Juan de Fuca Ridge. *Geochemistry, Geophysics, Geosystems*, *5*(1), Q01004. https://doi.org/10.1029/2003GC000604

Bohnenstiehl, D. R., Waldhauser, F., & Tolstoy, M. (2008). Frequency-magnitude distribution of microearthquakes beneath the 9°50'N region of the East Pacific Rise, October 2003 through April 2004. *Geochemistry, Geophysics, Geosystems*, *9*(10), Q10T03. https://doi.org/10.1029/2008GC002128

Bohrmann, G., & dos Santos Ferreira, C. (2018). MSM57/2 raw data of EM1002 multibeam echosounder (bathymetry & beam time series). *PANGAEA*. https://doi.org/10.1594/PANGAEA.895668

Bohrmann, G., & Wintersteller, P. (2018). MSM57/1 raw data of EM122 multibeam echosounder (bathymetry, beam time series & water column data). PANGAEA. https://doi.org/10.1594/PANGAEA.895661

Buck, W. R., Einarsson, P., & Brandsdóttir, B. (2006). Tectonic stress and magma chamber size as controls on dike propagation: Constraints from the 1975–1984 Krafla rifting episode. *Journal of Geophysical Research: Solid Earth*, *111*(B12). https://doi.org/10.1029/2005JB003879

Cannat, M. (1996). How thick is the magmatic crust at slow spreading oceanic ridges? *Journal of Geophysical Research: Solid Earth*, *101*(B2), 2847–2857. https://doi.org/10.1029/95JB03116

Cannat, M., Rommevaux-Jestin, C., & Fujimoto, H. (2003). Melt supply variations to a magma-poor ultra-slow spreading ridge (Southwest Indian Ridge 61° to 69°E). *Geochemistry, Geophysics, Geosystems*, *4*(8), 9104. https://doi.org/10.1029/2002GC000480

Christensen, N. I. (1996). Poisson's ratio and crustal seismology. *Journal of Geophysical Research: Solid Earth*, *101*(B2), 3139–3156. https://doi.org/10.1029/95JB03446

Combier, V., Seher, T., Singh, S. C., Crawford, W. C., Cannat, M., Escartín, J., & Dusunur, D. (2015). Three-dimensional geometry of axial magma chamber roof and faults at Lucky Strike Volcano on the Mid-Atlantic Ridge. *Journal of Geophysical Research: Solid Earth*, *120*(8), 5379–5400. https://doi.org/10.1002/2015JB012365

Connelly, D. P., German, C. R., Asada, M., Okino, K., Egorov, A., Naganuma, T., et al. (2007). Hydrothermal activity on the ultra-slow spreading southern Knipovich Ridge. *Geochemistry, Geophysics, Geosystems*, *8*(8), Q08013. https://doi.org/10.1029/2007GC001652

Curewitz, D., Okino, K., Asada, M., Baranov, B., Gusev, E., & Tamaki, K. (2010). Structural analysis of fault populations along the oblique, ultra-slow spreading Knipovich Ridge, North Atlantic Ocean, 74°30′N-77°50′N. *Journal of Structural Geology*, *32*(6), 727–740. https://doi.org/10.1016/j.jsg.2009.08.011

Dahm, T. (2000). Numerical simulations of the propagation path and the arrest of fluid-filled fractures in the Earth. *Geophysical Journal International*, *141*(3), 623–638. https://doi.org/10.1046/j.1365-246x.2000.00102.x

Damm, V., Franke, D., & Wölfl, A.-C. (2018). Raw multibeam EM122 data: Transits of Maria S. Merian cruise MSM67 (North Atlantic). PANGAEA. https://doi.org/10.1594/PANGAEA.892814

DeMets, C., Gordon, R. G., & Argus, D. F. (2010). Geologically current plate motions. *Geophysical Journal International*, *181*(1), 1–80. https://doi.org/10.1111/j.1365-246X.2009.04491.x

Dick, H. J. B., Lian, J., & Schouten, H. (2003). An ultraslow-spreading class of ocean ridge. *Nature*, *426*(6965), 405–412. https://doi.org/10.1038/nature02128

Dunn, R. A., Arai, R., Eason, D. E., Canales, J. P., & Sohn, R. A. (2017). Three-dimensional seismic structure of the Mid-Atlantic Ridge: An investigation of tectonic, magmatic, and hydrothermal processes in the rainbow area. *Journal of Geophysical Research: Solid Earth*, *122*(12), 9580–9602. https://doi.org/10.1002/2017JB015051

Dunn, R. A., & Forsyth, D. W. (2007). Crust and lithospheric structure - seismic structure of Mid-Ocean Ridges. In G. Schubert (Ed.), *Treatise on Geophysics* (1st ed., pp. 419–443). Elsevier Science.

Dunn, R. A., Lekić, V., Detrick, R. S., & Toomey, D. R. (2005). Three-dimensional seismic structure of the Mid-Atlantic Ridge (35°N): Evidence for focused melt supply and lower crustal dike injection. *Journal of Geophysical Research: Solid Earth*, *110*(B9), B09101. https://doi.org/10.1029/2004JB003473

Dunn, R. A., Toomey, D. R., & Solomon, S. C. (2000). Three-dimensional seismic structure and physical properties of the crust and shallow mantle beneath the East Pacific Rise at 9°30'N. *Journal of Geophysical Research: Solid Earth*, *105*(B10), 23537–23555. https://doi.org/10.1029/2000JB900210

Elkins, L. J., Sims, K. W. W., Prytulak, J., Blichert-Toft, J., Elliott, T., Blusztajn, J., et al. (2014). Melt generation beneath Arctic ridges: Implications from U decay series disequilibria in the Mohns, Knipovich, and Gakkel Ridges. *Geochimica et Cosmochimica Acta*, *127*, 140–170. https://doi.org/10.1016/j.gca.2013.11.031

Essing, D., Schlindwein, V., Schmidt-Aursch, M. C., Hadziioannou, C., & Stähler, S. C. (2021). Characteristics of current-induced harmonic tremor signals in ocean-bottom seismometer records. *Seismological Research Letters*, *92*(5), 3100–3112. https://doi.org/10.1785/0220200397

German, C. R., Baker, E. T., Mevel, C., Tamaki, K., & FUJI Science Team. (1998). Hydrothermal activity along the Southwest Indian Ridge. *Nature*, *395*(6701), 490–493. https://doi.org/10.1038/26730

Greenfield, T., White, R. S., & Roecker, S. (2016). The magmatic plumbing system of the Askja Central Volcano, Iceland, as imaged by seismic tomography. *Journal of Geophysical Research: Solid Earth*, *121*(10), 7211–7229. https://doi.org/10.1002/2016JB013163

Hahm, D., Postlethwaite, C. F., Tamaki, K., & Kim, K.-R. (2004). Mechanisms controlling the distribution of helium and neon in the Arctic seas: The case of the Knipovich Ridge. *Earth and Planetary Science Letters*, *229*(1–2), 125–139. https://doi.org/10.1016/j.epsl.2004.10.028

Hammond, W. C., & Humphreys, E. D. (2000). Upper mantle seismic wave velocity: Effects of realistic partial melt geometries. *Journal of Geophysical Research: Solid Earth*, *105*(B5), 10975–10986. https://doi.org/10.1029/2000JB900041

Hellevang, B., & Pedersen, R. B. (2005). Magmatic segmentation of the northern Knipovich Ridge: Evidence for high-pressure fractionation at an ultraslow spreading ridge. *Geochemistry, Geophysics, Geosystems*, *6*(9), Q09007. https://doi.org/10.1029/2004GC000898

Indrastuti, N., Nugraha, A. D., McCausland, W. A., Hendrasto, M., Gunawan, H., Kusnandar, R., et al. (2019). 3-D seismic tomographic study of Sinabung volcano, Northern Sumatra, Indonesia, during the inter-eruptive period October 2010–July 2013. *Journal of Volcanology and Geothermal Research*, *382*, 197–209. https://doi.org/10.1016/j.jvolgeores.2019.03.001

Jeddi, Z., Ottemöller, L., Sørensen, M. B., Rezaei, S., Gibbons, S. J., Strømme, M. L., et al. (2021). Improved seismic monitoring with OBS deployment in the Arctic: A pilot study from offshore Western Svalbard. *Seismological Research Letters*, *92*(5), 2705–2717. https://doi.org/10.1785/0220200471

Jokat, W., Ritzmann, O., Schmidt-Aursch, M. C., Drachev, S., Gauger, S., & Snow, J. (2003). Geophysical evidence for reduced melt production on the Arctic ultraslow Gakkel mid-ocean ridge. *Nature*, *423*(6943), 962–965. https://doi.org/10.1038/nature01706

Kim, E., Toomey, D. R., Hooft, E. E. E., Wilcock, W. S. D., Weekly, R. T., Lee, S.-M., & Kim, Y. (2019). Upper crustal Vp/Vs ratios at the endeavour segment, Juan de Fuca Ridge, from joint inversion of P and S traveltimes: Implications for hydrothermal circulation. *Geochemistry, Geophysics, Geosystems*, *20*(1), 208–229. https://doi.org/10.1029/2018GC007921

Kissling, E. (1995). *Program VELEST USER'S GUIDE - Short introduction*. Institute of Geophysics.

Korger, E. I. M., & Schlindwein, V. (2014). Seismicity and structure of the 85°E volcanic complex at the ultraslow spreading Gakkel Ridge from local earthquake tomography. *Geophysical Journal International*, *196*(1), 539–551. https://doi.org/10.1093/gji/ggt390

Koulakov, I. (2009). LOTOS code for local earthquake tomographic inversion. Benchmarks for testing tomographic algorithms. *Bulletin of the Seismological Society of America*, *99*(1), 194–214. https://doi.org/10.1785/0120080013

Koulakov, I., Abkadyrov, I., Al Arifi, N., Deev, E., Droznina, S., Gordeev, E. I., et al. (2017). Three different types of plumbing system beneath the neighboring active volcanoes of Tolbachik, Bezymianny, and Klyuchevskoy in Kamchatka. *Journal of Geophysical Research: Solid Earth*, *122*(5), 3852–3874. https://doi.org/10.1002/2017JB014082

Koulakov, I., Boychenko, E., & Smirnov, S. Z. (2020). Magma chambers and meteoric fluid flows beneath the Atka volcanic complex (Aleutian Islands) inferred from local earthquake tomography. *Geosciences*, *10*(6), 214. https://doi.org/10.3390/geosciences10060214

Koulakov, I., Komzeleva, V., Smirnov, S. Z., & Bortnikova, S. B. (2021). Magma-fluid interactions beneath Akutan volcano in the Aleutian arc based on the results of local earthquake tomography. *Journal of Geophysical Research: Solid Earth*, *126*(3), e2020JB021192. https://doi.org/10.1029/2020JB021192

Kvarven, T., Hjelstuen, B. O., & Mjelde, R. (2014). Tectonic and sedimentary processes along the ultraslow Knipovich spreading ridge. *Marine Geophysical Research*, *35*(2), 89–103. https://doi.org/10.1007/s11001-014-9212-1

Liu, Y., Tao, C., Liu, C., Qiu, L., Schlindwein, V., Zhang, H., et al. (2019). Seismic activity recorded by a single OBS/H near the active Longqi hydrothermal vent at the ultraslow spreading Southwest Indian Ridge (49°39′ E). *Marine Georesources & Geotechnology*, *37*(2), 201–211. https://doi.org/10.1080/1064119X.2017.1420114

McKenzie, D., Jackson, J., & Priestly, K. (2005). Thermal structure of oceanic and continental lithosphere. *Earth and Planetary Science Letters*, *233*(3–4), 337–349. https://doi.org/10.1016/j.epsl.2005.02.005

Meier, M., & Schlindwein, V. (2018). First in situ seismic record of spreading events at the ultraslow spreading Southwest Indian Ridge. *Geophysical Research Letters*, *45*(19), 10360–10368. https://doi.org/10.1029/2018GL079928

Meier, M., & Schlindwein, V. (2022). Microearthquake phase picks at the Knipovich Ridge 75.5-77.5N from 2016-09 till 2017-07. *PANGAEA*. https://doi.org/10.1594/PANGAEA.947271

Meier, M., Schlindwein, V., & Scholz, J.-R. (2020). Microearthquake catalogue at the Knipovich Ridge 75.5-77.5N from 2016-09 till 2017-07. *PANGAEA*. https://doi.org/10.1594/PANGAEA.924065

Meier, M., Schlindwein, V., Scholz, J.-R., Geils, J., Schmidt-Aursch, M. C., Krüger, F., et al. (2021). Segment-scale seismicity of the ultraslow spreading Knipovich Ridge. *Geochemistry, Geophysics, Geosystems*, *22*(2), e2020GC009375. https://doi.org/10.1029/2020GC009375

Mendel, V., Sauter, D., Rommevaux-Jestin, C., Patriat, P., Lefebvre, F., & Parson, L. M. (2003). Magmato-tectonic cyclicity at the ultra-slow spreading Southwest Indian Ridge: Evidence from variations of axial volcanic ridge morphology and Abyssal hills pattern. *Geochemistry, Geophysics, Geosystems*, *4*(5), 9102. https://doi.org/10.1029/2002GC000417

Michael, P. J., Langmuir, C. H., Dick, H. J. B., Snow, J. E., Goldstein, S. L., Graham, D. W., et al. (2003). Magmatic and amagmatic seafloor generation at the ultraslow-spreading Gakkel Ridge, Arctic Ocean. *Nature*, *423*(6943), 956–961. https://doi.org/10.1038/nature01704

Montési, L. G. J., Behn, M. D., Hebert, L. B., Lin, J., & Barry, J. L. (2011). Controls on melt migration and extraction at the ultraslow Southwest Indian Ridge 10°–16°E. *Journal of Geophysical Research: Solid Earth*, *116*(B10), B10102. https://doi.org/10.1029/2011JB008259

Müller, C., & Jokat, W. (2011). Seismic evidence for volcanic activity discovered in central Arctic. *EOS*, *81*(24), 265–269. https://doi.org/10.1029/00eo00186

Okino, K., Curewitz, D., Asada, M., Tamaki, K., Vogt, P., & Crane, K. (2002). Preliminary analysis of the Knipovich Ridge segmentation: Influence of focused magmatism and ridge obliquity on an ultraslow spreading system. *Earth and Planetary Science Letters*, *202*(2), 275–288. https://doi.org/10.1016/S0012-821X(02)00790-2

Paquet, M., Cannat, M., Brunelli, D., Hamelin, C., & Humler, E. (2016). Effect of melt/mantle interactions on MORB chemistry at the easternmost Southwest Indian Ridge (61°–67°E). *Geochemistry, Geophysics, Geosystems*, *17*(11), 4605–4640. https://doi.org/10.1002/2016GC006385

Pedersen, R. B., Rapp, H. T., Thorseth, I. H., Lilley, M. D., Barriga, F. J. A. S., Baumberger, T., et al. (2010). Discovery of a black smoker vent field and vent fauna at the Arctic Mid-Ocean Ridge. *Nature Communications*, *1*(1), 126. https://doi.org/10.1038/ncomms1124

Pontbriand, C. W., Soule, S. A., Sohn, R. A., Humphris, S. E., Kunz, C., Singh, H., et al. (2012). Effusive and explosive volcanism on the ultraslow-spreading Gakkel Ridge, 85°E. *Geochemistry, Geophysics, Geosystems*, *13*(10), Q10005. https://doi.org/10.1029/2012gc004187

Rickers, F., Fichtner, A., & Trampert, J. (2013). The Iceland–Jan Mayen plume system and its impact on mantle dynamics in the North Atlantic region: Evidence from full-waveform inversion. *Earth and Planetary Science Letters*, *367*, 39–51. https://doi.org/10.1016/j.epsl.2013.02.022

Sauter, D., & Cannat, M. (2010). The ultraslow spreading Southwest Indian Ridge. In P. A. Rona, C. W. Devey, J. Dyment, & B. J. Murton (Eds.), *Diversity of hydrothermal systems on slow spreading ocean ridges* (Vol. 188, pp. 153–173). American Geophysical Union.

Sauter, D., Parson, L., Mendel, V., Rommevaux-Jestin, C., Gomez, O., Briais, A., et al. (2002). TOBI sidescan sonar imagery of the very slow-spreading Southwest Indian Ridge: Evidence for along-axis magma distribution. *Earth and Planetary Science Letters*, *199*(1–2), 81–95. https://doi.org/10.1016/S0012-821X(02)00543-5

Sauter, D., Patriat, P., Rommevaux-Jestin, C., Cannat, M., & Briais, A., & Gallieni Shipboard Scientific Party. (2001). The Southwest Indian Ridge between 49°15′E and 57°E: Focused accretion and magma redistribution. *Earth and Planetary Science Letters*, *192*(3), 303–317. https://doi.org/10.1016/S0012-821X(01)00455-1

Schlindwein, V. (2012). Teleseismic earthquake swarms at ultraslow spreading ridges: Indicator for dyke intrusions? *Geophysical Journal International*, *190*(1), 442–456. https://doi.org/10.1111/j.1365-246X.2012.05502.x

Schlindwein, V., Demuth, A., Geissler, W. H., & Jokat, W. (2013). Seismic gap beneath Logachev seamount: Indicator for melt focusing at an ultraslow mid-ocean ridge? *Geophysical Research Letters*, *40*(9), 1703–1707. https://doi.org/10.1002/grl.50329

Schlindwein, V., Krüger, F., & Schmidt-Aursch, M. (2018). Project KNIPAS: DEPAS ocean-bottom seismometer operations in the Greenland Sea in 2016-2017. *PANGAEA*. https://doi.org/10.1594/PANGAEA.896635

Schlindwein, V., & Schmid, F. (2016). Mid-ocean-ridge seismicity reveals extreme types of ocean lithosphere. *Nature*, *535*(7611), 276–279. https://doi.org/10.1038/nature18277

Schlindwein, V., & Wölfl, A.-C. (2018). Raw multibeam EM122 data of Maria S. Merian cruise MSM68 (North Atlantic). *PANGAEA*. https://doi.org/10.1594/PANGAEA.892679

Schmid, F., & Schlindwein, V. (2016). Microearthquake activity, lithospheric structure, and deformation modes at an amagmatic ultraslow spreading Southwest Indian Ridge segment. *Geochemistry, Geophysics, Geosystems*, *17*(7), 2905–2921. https://doi.org/10.1002/2016GC006271

Schmid, F., Schlindwein, V., Koulakov, I., Plötz, A., & Scholz, J.-R. (2017). Magma plumbing system and seismicity of an active mid-ocean ridge volcano. *Scientific Reports*, *7*(1), 42949. https://doi.org/10.1038/srep42949

Schuler, J., Greenfield, T., White, R. S., Roecker, S. W., Brandsdóttir, B., Stock, J. M., et al. (2015). Seismic imaging of the shallow crust beneath the Krafla Central Volcano, NE Iceland. *Journal of Geophysical Research: Solid Earth*, *120*(10), 7156–7173. https://doi.org/10.1002/2015JB012350

Schweitzer, J. (2001). HYPOSAT - An enhanced routine to locate seismic events. *Pure and Applied Geophysics*, *158*(1), 277–289. https://doi.org/10.1007/PL00001160

Schweitzer, J. (2018). User manual HYPOSAT 6 and HYPOMOD 2.

Singh, S. C., Crawford, W. C., Carton, H., Seher, T., Combier, V., Cannat, M., et al. (2006). Discovery of a magma chamber and faults beneath a Mid-Atlantic Ridge hydrothermal field. *Nature*, *442*(7106), 1029–1032. https://doi.org/10.1038/nature05105

Sohn, R. A., Hildebrand, J. A., Webb, S. C., & Fox, C. G. (1995). Hydrothermal microseismicity at the megaplume site on the Southern Juan de Fuca Ridge. *Bulletin of the Seismological Society of America*, *85*(3), 775–786. https://doi.org/10.1785/BSSA0850030775

Standish, J. J., Dick, H. J. B., Michael, P. J., Melson, W. G., & O'Hearn, T. (2008). MORB generation beneath the ultraslow spreading Southwest Indian Ridge (9–25°E): Major element chemistry and the importance of process versus source. *Geochemistry, Geophysics, Geosystems*, *9*(5), Q05004. https://doi.org/10.1029/2008GC001959

Sundvor, E. (1997). Joint U.S., Russian and Norwegian research at Knipovich Ridge, Norwegian-Greenland Sea. *InterRidge News*, *6*(1), 17.

Syracuse, E. M., Maceira, M., Zhang, H., & Thurber, C. H. (2015). Seismicity and structure of Akutan and Makushin Volcanoes, Alaska, using joint body and surface wave tomography. *Journal of Geophysical Research: Solid Earth*, *120*(2), 1036–1052. https://doi.org/10.1002/2014JB011616

Takei, Y. (2002). Effect of pore geometry on Vp/Vs: From equilibrium geometry to crack. *Journal of Geophysical Research: Solid Earth*, *107*(B2), 2043. https://doi.org/10.1029/2001JB000522

Tamaki, K., Cherkashev, G., & Team, K. K. (2001). Japan-Russia cooperation at the Knipovich Ridge in the Arctic Sea. *InterRidge News*, *10*(1), 48–52.

Tarasewicz, J., Brandsdóttir, B., White, R. S., Hensch, M., & Thorbjarnardóttir, B. (2012). Using microearthquakes to track repeated magma intrusions beneath the Eyjafjallajökull Stratovolcano, Iceland. *Journal of Geophysical Research*, *117*(B9), B00C06. https://doi.org/10.1029/2011JB008751

Tolstoy, M., Bohnenstiehl, D. R., Edwards, M. H., & Kurras, G. J. (2001). Seismic character of volcanic activity at the ultraslow-spreading Gakkel Ridge. *Geology*, *29*(12), 1139–1142. https://doi.org/10.1130/0091-7613(2001)029<1139:SCOVAA>2.0.CO;2

Toomey, D. R., Jousselin, D., Dunn, R. A., Wilcock, W. S. D., & Detrick, R. S. (2007). Skew of mantle upwelling beneath the East Pacific Rise governs segmentation. *Nature*, *446*(7134), 409–414. https://doi.org/10.1038/nature05679

Weekly, R. T., Wilcock, W. S. D., Toomey, D. R., Hooft, E. E. E., & Kim, E. (2014). Upper crustal seismic structure of the Endeavour segment, Juan de Fuca Ridge from traveltime tomography: Implications for oceanic crustal accretion. *Geochemistry, Geophysics, Geosystems*, *15*(4), 1296–1315. https://doi.org/10.1002/2013GC005159